Sondre Braathen Hafnor

Fatigue evaluation of notched Al-Si-10Mg produced by SLM

Master's thesis in Mechanical Engineering
Supervisor: Filippo Berto
June 2019

Master's thesis

NTNU
Kunnskap for en bedre verden

Sondre Braathen Hafnor

Fatigue evaluation of notched Al-Si-10Mg produced by SLM

Master's thesis in Mechanical Engineering
Supervisor: Filippo Berto
June 2019

Norwegian University of Science and Technology
Faculty of Engineering
Department of Mechanical and Industrial Engineering

NTNU
Kunnskap for en bedre verden

Fatigue evaluation of notched Al-Si-10Mg produced by SLM

Sondre Braathen Hafnor

June 2019

Abstract

In this work, the notch effect of additive manufactured Al-Si-10Mg is examined. An understanding of the theory is developed through a literature review with focus on the manufacturing process, alloy properties, fatigue life and heat treatment. Experiments are carried out to get values for the notch sensitivity of the material and to identify crack initiation mechanisms, both for as-build and heat treated samples. An experimental approach to defect evaluation is undertaken, which reveals some potential for new methods of measurement. Finally, some suggestions for the development of a production standard are presented.

Contents

1   Introduction

Additive Manufacturing is increasingly becoming a part of industry, and has by Klaus Schwab [26] been predicted to play a major role in what he calls *The Fourth Industrial revolution.* The purpose of this work is to aid in the development of this new technology.

1.1   Background and motivation

In a world where technological development is accelerating at a rapid pace, and the need for sustainable production methods are increasingly important, the role of Additive Manufacturing has come forth as a lucrative manufacturing method. It offers production with close to zero waste combined with the opportunity of complex designs, without the need for any preparation before production. Working towards a reliable production standard will further benefit this technology, thus providing a small piece to the puzzle that is Additive Manufacturing.

1.2   Problem description

The mechanical properties of AM parts is not yet well understood. This is especially true for aluminum, as to the authors best knowledge, no research on notch sensitivity of Al-Si-10Mg has been preformed. Further, the literature on defect analysis in additive manufactured metals varies a lot in method. The problems investigated in this work is therefore defined as follows:

1. Develop an empiric value for notch sensitivity of Al-Si-10Mg produced by selective laser melting.

2. Determine an analysis method of fracture surfaces to improve fatigue life predictions.

The overall goal is to establish a basic understanding of the behaviour of Al-Si-10Mg produced by Selective Laser Melting, with respect to notched fatigue strength.

1.3   Project scope

In this work, a series of fatigue life tests of SLM produced Al-Si-10Mg is undertaken. Smooth samples and notched samples are compared to determine the notch sensitivity.

1.3.1   Objectives

- Produce values for the notch sensitivity of the alloy

- Identify failure mechanisms in the samples

- Develop ideas for enhancing fatigue life of the alloy

2 Literature review

In this chapter, the initial research will be presented. This represents the relevant theory associated with the experiments presented in Section 3. It also aims to give some context as to why these experiments are preformed, and look at present and future applications of the alloy evaluated. The production method, Additive Manufacturing (AM), is focused on quite extensively in this work. AM is currently changing the rules of product development, both with respect to manufacturing and new product development [31]. The rapid adaptation of this revolutionary technology in industry makes it an interesting area of research, as the demand for improvements are high and many material and geometrical challenges remains unsolved.

2.1 Aluminum-silicon alloys

Aluminum-Silicon alloys were the main focus of the initial literature review, especially additive manufacturing of these alloys with respect to production of solar cells. It was, however, discovered that very little research has been done on this area. Solar application has therefore not been subject to further study.
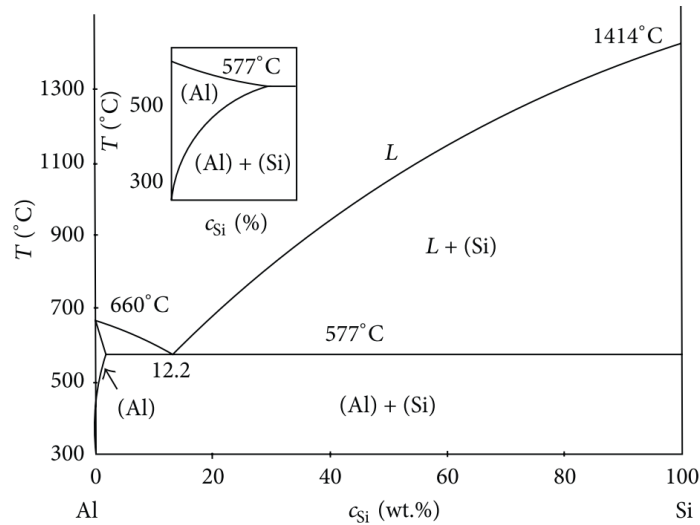

Figure 1: Aluminum-Silicon phase diagram. Figure from [3].

As seen in Figure 1, the eutectic point of Al-Si occurs around 12.2 wt.% at a temperature of 577°C [12]. The melting temperature of low wt.% of silicon is substantially lower than that of a high amount of silicon. This encourages the use of alloys with a low amount of silicon, as the manufacturing process will require less energy to heat the alloy. This is especially true for traditional production methods like casting, but also for AM. Al-Si alloys are commonly used in industry, due to its low weight, relatively high strength, excellent corrosion resistance and good machinability [18].

2.1.1 Al-Si-10Mg

Adding magnesium to the Al-Si alloy enables precipitation of Mg_2Si. This strengthens the matrix of the alloy, while not compromising other mechanical properties [18]. Al-Si-10Mg

is therefore a common aluminum alloy for a variety of applications, like aerospace and the automotive industry.

Table 1: Mechanical properties of Al-Si alloys. HPDC = High Pressure Die Casting. T6 = T6 heat treatment (Sec. 2.5.5). HV = Vickers Hardness, ε_f = elongation at fracture. Values from [30] and [18].

Alloy, method	E (GPa)	UTS (MPa)	ε_f	HV
Al-12Si, cast	-	177-207	8.5-9.5	-
Al-Si-10Mg, cast	71	300-317	2.5-3.5	86
Al-Si-10Mg, HPDC	71	300-350	3.0-5.0	95-105
Al-Si-10Mg, HPDC-T6	71	330-365	3.0-5.0	130-133

Looking at the different alloys and production methods in Table 1, it is observed that the inclusion of magnesium greatly improves Ultimate Tensile Strength (UTS), but also reduces the elongation at failure. It is known (and discussed in Section 2.5) that the ductility can be improved by heat treatment, at least in the case of production by Selective Laser Melting.

2.2 Additive manufacturing

Additive manufacturing (AM) of metals is an expensive process compared to other production methods [16][7]. This limits the commercial use of this technology to complex parts where traditional machining is even more expensive, or impossible. These parts are typically made from high strength materials like titanium alloys. As a result of this, much of the research done on the mechanical properties from AM methods is focused on titanium alloys, and more specifically Ti-6Al-4V [34]. Some of the research presented in this chapter is therefore focused on this specific alloy, as it forms a basic understanding of the mechanics, possibilities and challenges related to additive manufacturing of metals.

Another disadvantage of AM compared to conventional manufacturing processes is build speed with respect to volume. While machining or injection molding has reported process rates of over 100 kg/h, additive manufacturing operates at typically less than 100 g/h [34]. This extreme difference in process rates suggests - again - that AM applications should mainly focus on low volume parts with complex geometry, or low volume products, since AM benefits less from economics of scale than for example casting or extrusion. However, the advantages held by AM like on-demand production, zero material waste and virtually no restructuring cost makes it desirable to further develop this technology. For example, AM of metals has in the authors opinion great potential within the area of prototyping, as some advanced prototypes would require the use of metals to achieve better feedback during the product development process.

2.2.1 Powder bed system

Powder bed systems (Figure 2) consists of two chambers, one with the powder storage and one with the build volume. As the process starts, a roller moves a thin layer of metal powder from the powder storage to the powder bed. The energy source then melts the powder in the shape of the first layer of the design. This procedure is repeated for every layer of the component, until the three dimensional object is complete [16].
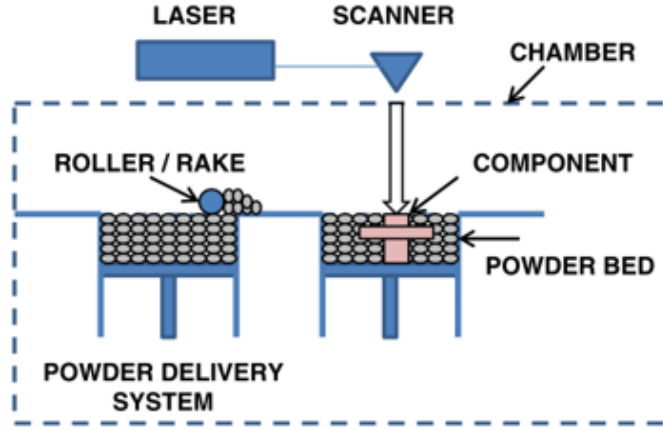
Figure 2: Illustration of a powder bed AM system. Figure from [16].

The powder surrounding the object works as support for geometry that otherwise would collapse, thus removing the need for additional support material that potentially could affect surface quality. This makes the powder bed method well suited for high resolution features, designs with internal passages and complex geometries. However, since the powder has to fill the entirety of the build volume (up to the last layer), the build volumes of this method are typically less than 0.03 m^3 [16].

2.2.2 Powder feed system

Powder feed systems (Figure 3) are quite similar to the powder bed system, but instead of letting the metal powder cover the whole build area, a deposition head guides the powder to only cover the area included in the respective layer of the design. This allows for less material use during production, but removes the support function of the leftover powder.
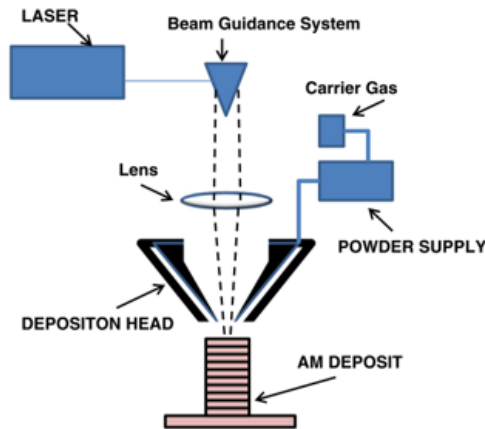

Figure 3: Illustration of a powder feed AM system. Figure from [16].

The reduction in required powder usage gives this method quite large build volumes of around 1 m^3. Another advantage of this method it that it is possible to add to existing

components, making it viable for repair and modification [16].

2.2.3 Wire feed system

Wire feed systems (Figure 4) are quite similar to welding. A wire of the metal is fed onto the work layer where it melts onto the previous layer. This method is fast, but not as precise as the powder based solutions, thus often requires additional post processing. The build volume of wire feed systems is in the range of 1 m^3 [16].
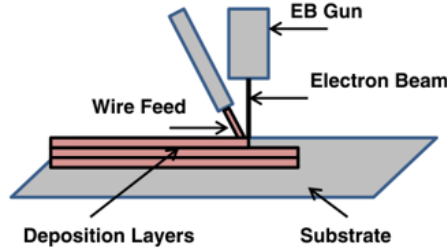

Figure 4: Illustration of a wire feed AM system. Figure from [16].

2.2.4 Energy sources

The most common production method in AM today is Selective Laser Melting (SLM), or Selective Laser Sintering (SLS). This method utilizes a fiber laser to melt or sinter the powder, and typically operates with a low power of 200-1000 W [16]. The build chamber is filled with a gas to minimize oxygen in the environment, thus reducing risk of hydrogen pick up [27]. SLM typically operates at high scanning speeds which leads to high cooling rates. This results in non-equilibrium microstructure which might require heat treatment for certain applications. High cooling rates can also cause residual stresses, thus compromising the mechanical properties of the part [22]. This problem can be counteracted to some degree by pre-heating the chamber to reduce cooling rates.

Another common technology is Electron Beam Melting (EBM). This method heats the powder by kinetic energy in the form of an electron beam, which penetrates multiple times deeper than a laser beam and can therefore not produce layers as thin as the SLM technology. For the electron beam to work, the chamber needs to be in a near vacuum state. This also prevents oxygen from interfering with the melt. In EBM, the process starts with a pre-heating of the powder. This is done by the electron beam at a very high scan speed, large focal spot and a low beam current [22]. This heating lowers the moisture in the powder, thus further reducing the oxygen interference. More importantly, the pre-heating reduces the local cooling rate, thus reducing residual stress buildup.

To highlight the differences between SLM and EBM, a concrete comparison is presented in Table 2. Note that the values presented in this table are example values, and adjusting different production parameters can change mechanical behaviour. However, the comparison does show a significant difference between the production methods, especially with respect to elongation and surface roughness. Note that even SLM produces a surface finish that is worse than most other production methods.

In the case of Al-Si-10Mg, there has (after the authors best knowledge) only been research done on samples produced by SLM. This might be a result of the difference in availability,

Table 2: Comparison between as-build SLM and EBM of Ti6Al4V alloy. SLM = Selective Laser Melting, EBM = Electron Beam Melting. R_a = Average surface roughness, σ_y = yield strength. Values from [22][33][15][16][10].

Properties	SLM	EBM
E (GPa)	94	118
UTS (MPa)	1250-1267	830-1150
σ_y (MPa)	1110-1125	915-1200
ε_f (%)	6-7	13-25
Micro-hardness (HV)	479-613	358-387
Side R_a (μm)	20-40	90-200

as the EBM method is a far less widespread than SLM [16].

2.2.5 Microstructure

As a result of the layer based production method of AM, the material experiences cyclic heating, as illustrated in Figure 5 [16]. This repeated heating has shown to produce a columnar microstructure (Figure 6) through the whole part in Ti-6Al-4V.
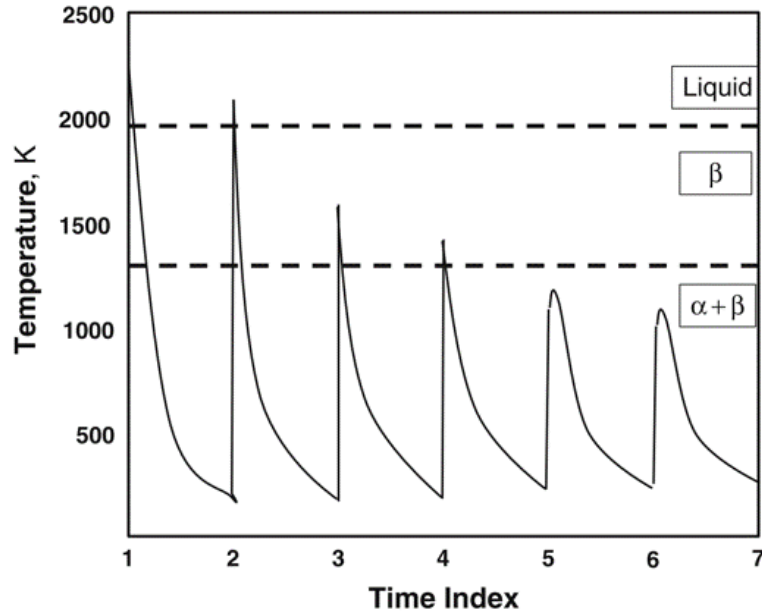

Figure 5: Thermal profile of a single layer of Ti-6Al-4V during AM. β: body-centered-cubic phase. α: hexagonal phase. Figure from [16].
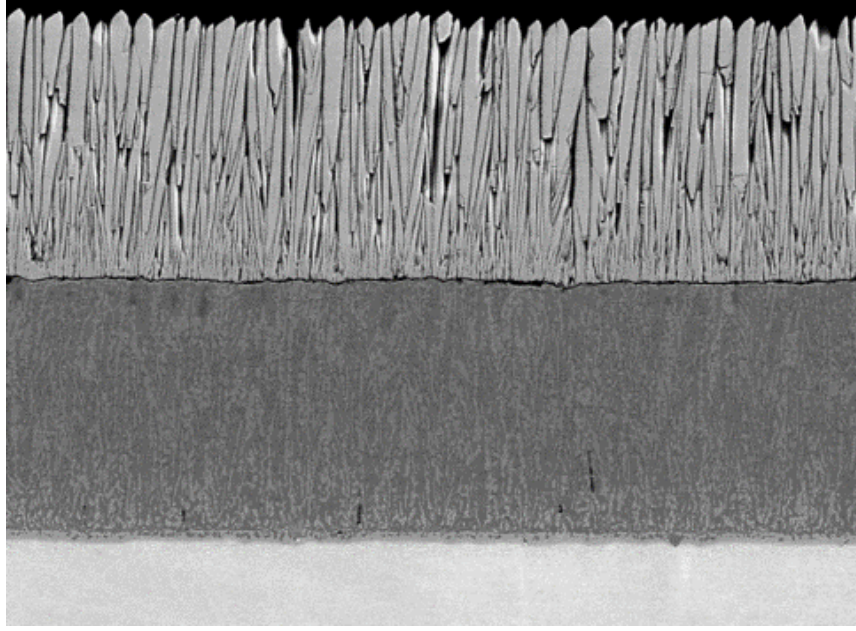
9

Figure 6: Columnar microstructure. Figure from [1].

This structure, while maintaining good yield and ultimate strength, is more brittle than the industry standard for the alloy. This can be explained by the formation of a fine microstructure as a result of the high cooling rate. However, heat treatment of the printed titanium alloy can improve ductility of the specimen significantly [34]. This is illustrated in Figure 7, where the mechanical strength of a titanium alloy is presented with two different heat treatment strategies. Note the difference in ductility in the transverse direction.
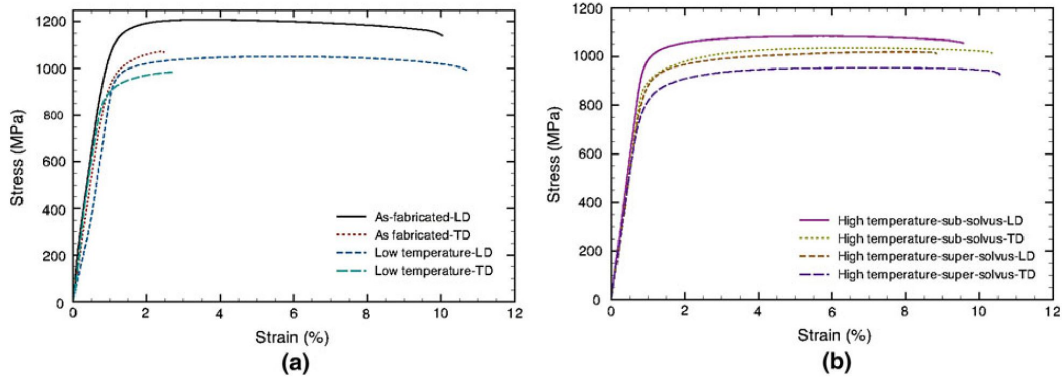
Figure 7: Stress-strain for SLM-printed Ti-6Al-4V with different heat treatments. Both Longitudinal Direction (LD) and Transverse Direction (TD) have been tested. (a) as-fabricated with low temperature strategy and (b) high temperature strategy with super- and subtransus treatment. Figure from [34].

This difference is credited to the manufacturing defects and specifically from lack of fusion, as seen in Figure 8. Small non-fused spots will act like internal cracks, thus affect the strength of the material, especially in the transverse direction [29].
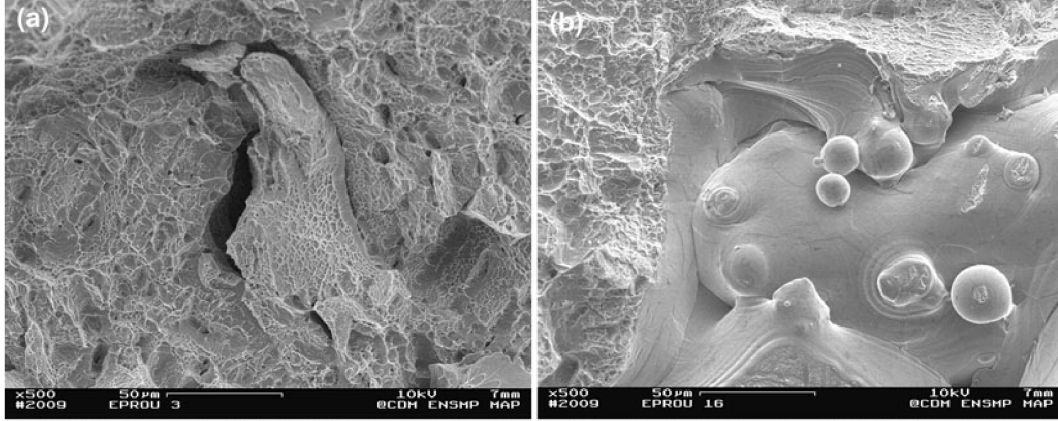
Figure 8: Fracture surfaces on tensile test specimens of as-fabricated microstructure. (a) longitudinal direction and (b) transverse direction. Figure from [34].

Eutectic Al-Si alloys has also been subject to research, with Selective Laser Melting (SLM) as production method [17][30]. It was shown that the density of the specimen was closely related to laser power (Figure 9). Low porosity (or high relative density) means less cavities and consequentially higher yield and ultimate strength.
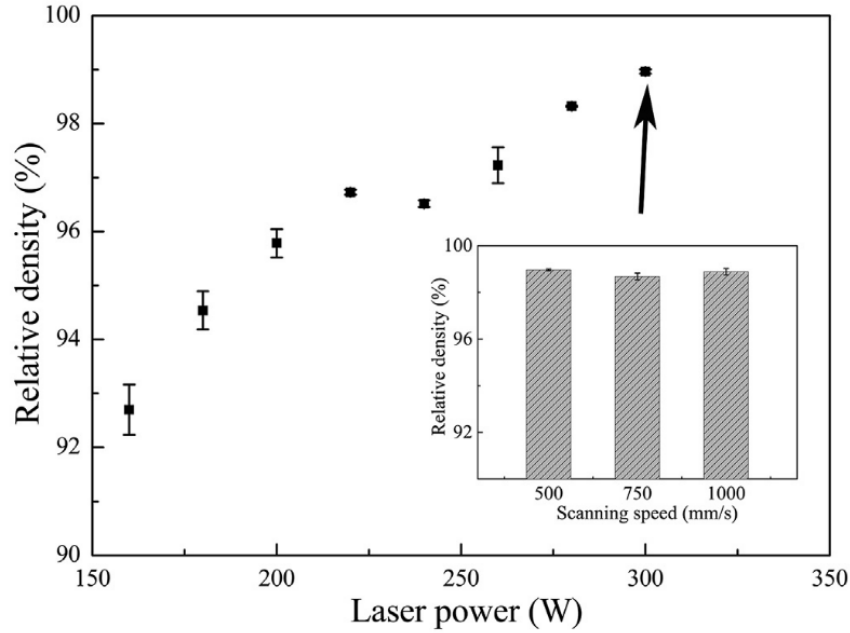
Figure 9: Relative density of SLM processed sample regarding laser power and scanning speed (inner picture). Figure from [17].

With in-situ alloy fabrication, the scanning speed still affected the final properties of the specimens. This was credited to insufficient melting of the silicon particles, resulting in partial melted Si and formation of Si groups. A high length/with ratio of interfaces of molten

pool was also reported to create stress concentration regions, thus giving the samples with high scanning speed a more brittle fracture.

The tests on SLM produced specimens with pre-alloyed powder were conducted with scanning speeds well above $1m/s$, yet it was reported an ultimate strength above (325 MPa) that of the in-situ produced Al-12Si (273 MPa). These results substantiates the conclusion that Si particles does not melt properly in the high scanning speed in-situ case. It was also reported that the pre-alloyed tensile test showed only small differences between longitudinal and transverse direction, as seen in Figure 11 [30]. This is in contrast to the difference in directional strength reported for the Ti-6Al-4V alloy. It is notable that the tensile strength of both the in-situ processed and the pre-alloyed samples was reported with much higher values than those from conventional cast specimens, which has an ultimate strength of about 192 MPa.
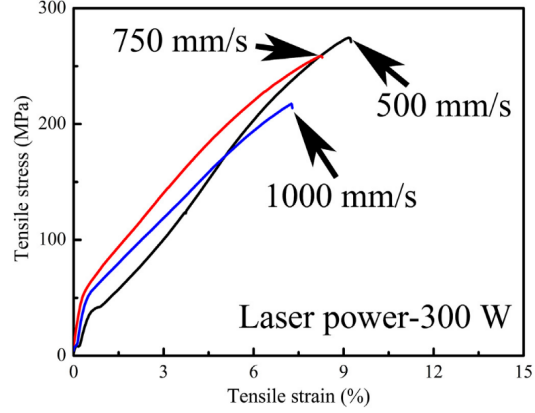

Figure 10: Stress-strain curve of SLM in-situ processed Al-12Si alloy under different laser scanning speeds. Figure from [17].

Table 3: Tensile properties of Selective Laser Melting specimens of Al-12Si. Values from [30] and [17]

Specimen	YS (MPa)	UTS (MPa)	$e_f(\%)$
Pre-alloyed $\parallel$	270	325	4.4
Pre-alloyed $\perp$	275	296	2.2
In-situ, 500 mm/s	-	273	9.5
In-situ, 1000 mm/s	-	217	6.5
Conventional cast	104	192	9.0

The drastic increase in material strength shown in Table 3 is mainly due to the ultrafine microstructure that forms as a result of the rapid cooling rate. The in-situ processed specimen at 500 mm/s has a much higher ultimate strength than the casted control values, while maintaining the ductility, thus creating the appearance of being the superior choice for most applications. Looking at Figure 10 however, it looks like most of the deformation is plastic deformation, but this is not discussed in the literature.

In the specific case of SLM produced Al-Si-10Mg, it was reported by S. Bagherifard et al. [6] that the microstructure of the as-build material was observed to be inhomogeneous. It was, in the transverse plane, noticeably coarser microstructure in the boundaries between molten pools. This could be a result of local variation in cooling rates, as cooling rate is known to be critical with respect to microstructure resolution. After heat treatment it was however observed that the microstructure became homogeneous, as the Si around the α-Al grains diffused to form particles that are homogeneously dispersed in the α-matrix.

2.2.6 Defects

Any structural deviations from intended production results are defined as defects in the material. The inclusion of defects in any material is unavoidable in practice. These defects reduce the mechanical properties compared to theoretical values, and the magnitude of defects should therefore be minimized. In AM, defects are often found to be high surface roughness, lack of fusion and gas inclusion, where the latter is usually parameterized by porosity.

In fatigue regarding AM samples, it is often observed that lack of fusion is the most common crack initiation mechanism [11]. Unfused areas can be evaluated as cracks, internal or at the surface, after the $\sqrt{area}$-method developed by Murakami in [20]. With this approach, the area of the defects is used to simulate a crack, using $\sqrt{area} = a$. The stress intensity of a crack tip can be written as

Figure 11: Stress-strain curve of SLM prealloyed Al-12Si in longitudinal (red) and transverse (blue) direction. Figure from [30].

$$K = \sigma Y \sqrt{\pi a} \tag{1}$$

where K is the stress intensity factor, σ is the applied stress, Y the crack geometry factor and a is the crack length derived from the defect area. For irregular shaped defects, as often found in AM parts, the real area is substituted with a slightly larger area with smooth corners. This new area is known as $area_{eff}$, and is considered more accurate for $\sqrt{area}$ evaluation than the actual $area$ [20][36]. For internal defects close to the surface and multiple surface defects in close proximity, an additional expansion of $area_{eff}$ should be considered after the criteria

$$If \quad e < d \rightarrow use \quad \sqrt{area_{eff}} \quad expanded$$
$$If \quad e1 < d2 \rightarrow use \quad \sqrt{area_{eff}} \quad expanded$$

where e is the distance from the surface to the defect, d is the height of the defect, $d2$ is the width of the smallest defect between two defects and $e1$ is the distance between the defects. See Figure 12.
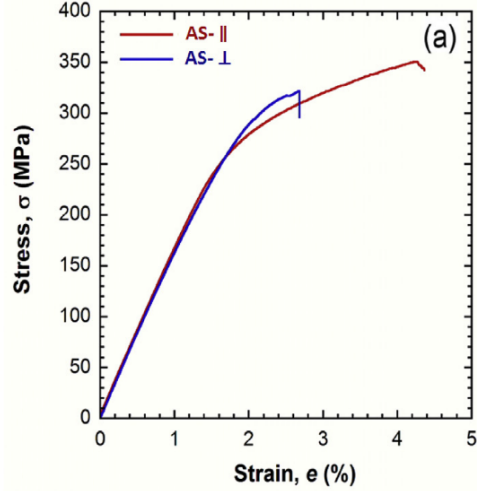
13

(a) Irregular defect at the surface.

(b) Internal irregular defect.

(c) Internal irregular defect close to the surface.

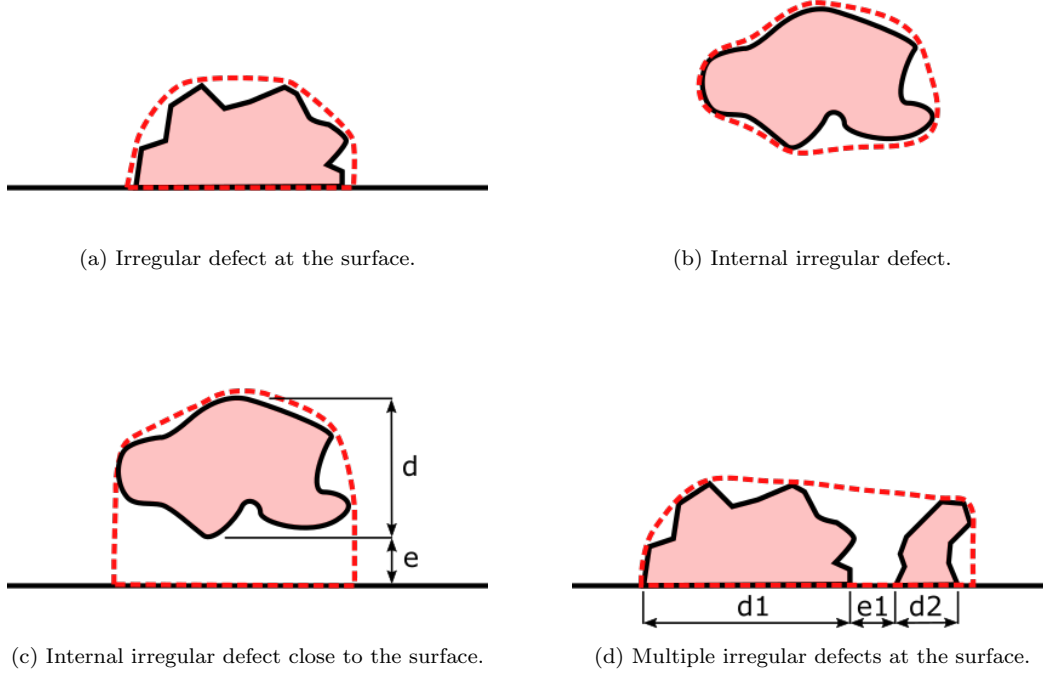(d) Multiple irregular defects at the surface.

Figure 12: Defect evaluation close to the surface after the $\sqrt{area}$-method. The pink area represents the original defect, while the dotted red line represents the effective area ($area_{eff}$). (c) and (d) illustrates $\sqrt{area_{eff}}$ expanded.

Simplifying the complex defects to be evaluated with standard fracture mechanics has proven to give accurate predictions of stress concentration, also in the case of AM[36].

2.2.7 Prototyping

Prototyping is the process of testing preliminary product designs as a method of validating assumptions made during product development. Additive manufacturing has been a central part of this in recent time, using Fused Deposition Modelling (FDM). The definition of the word *prototype* is not unambiguous in literature, but can be simplistically described as an approximation of a product or a function. The process of rapidly developing and testing prototypes has been established as the best practice in software development, as the short feedback loops allows for quick fixes and many incremental improvements over a short period of time. Mapping this onto physical prototypes, it is clear that the prototyping process will have a longer feedback loop, since the build time goes from seconds to hours or days, even with the use of AM. This does not disqualify this approach, but rather encourages more precise prototyping, thus making the number of needed iterations decrease [13]. The application of Additive Manufacturing in prototyping is therefore worth investigating, not only with respect to FDM, but also when evaluating applications of AM of metals.

Fused Deposition Modelling is an additive manufacturing method where the material

filament, usually polymer, is pushed through a hot nozzle, which melts the material. The nozzle moves relative to a build plate where the material is deposited. Layer profiles are drawn on top of each other until the model is finished. This is a popular, low-cost technology that is widely used in industry, but also by hobbyists and enthusiast. This widespread usage makes FDM a very important tool in global innovation and even production [32].

While FDM has a unique spot in the early to mid stages of product development, it is not as suited for final function prototypes, where the prototype needs to simulate the end product very closely, given that the end product will be made of metal. Utilizing AM of metals to create these prototypes has the potential to greatly reduce the cost and build time of these late stage prototypes, as it does not require the creation of expensive tools for this specific task. This was exemplified by Frazier [16] in Figure 13.
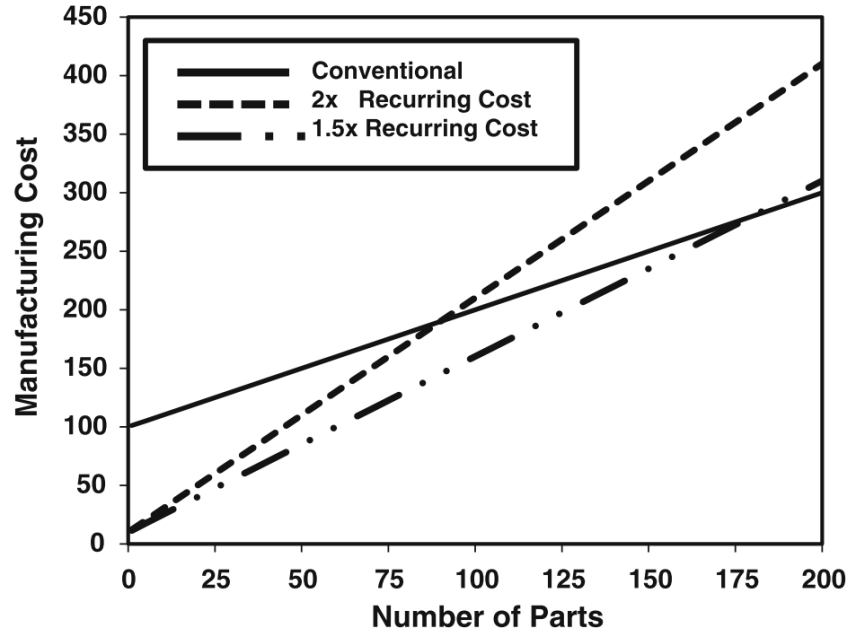
Figure 13: Example of cost using AM versus conventional production methods. Graph from [16].

Here it is assumed, based on the AM review performed, that the fixed costs of AM are one tenth of those of conventional manufacturing methods. Further it is assumed that the recurring costs are higher by an order of magnitude of 1.5 or 2.0, both shown in the graph. Even tho this is a rough estimate, it does highlight the value of AM with respect to low production series, thus showing the viability with respect to prototypes. Further development in AM technology is therefore considered by the author to be favorable not only for production purposes, but also for development of new products.

2.3   Fatigue

Components used in the real world quite often experience diverse load histories. One of the frequently occurring load characteristics is cyclic loading, which is a repetitive variation in load magnitude. Consider, as an example, a diving board. Even if it is designed to withstand jumps from people up to 150 kg, it is severely under dimensioned if it breaks after 10000

+-[H]
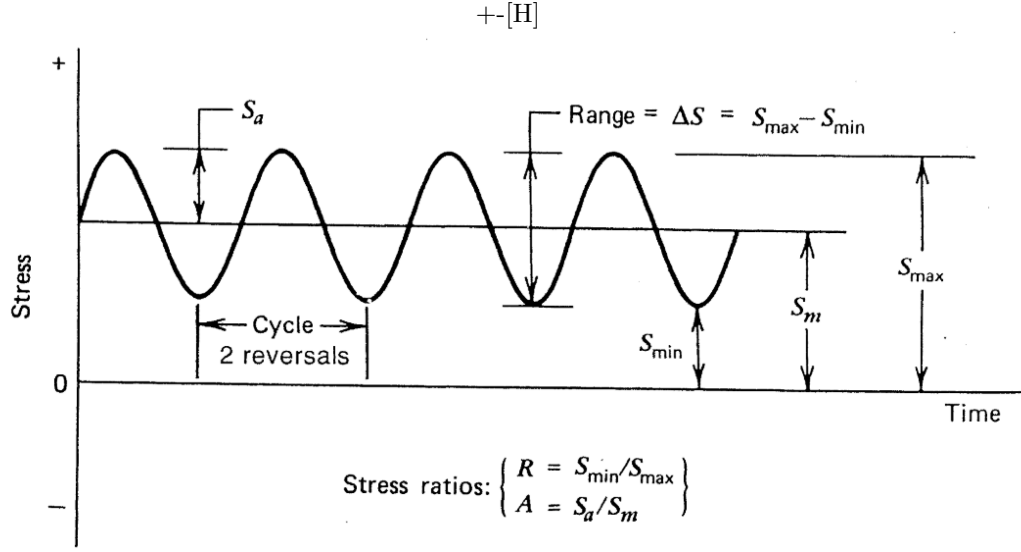
Figure 14: Illustration of constant amplitude cyclic loading. Figure from [23].

jumps from a person weighting 80 kg. This failure mechanism is called *fatigue* and is one of the more common failures seen in products today.

To evaluate fatigue life of materials and geometries, cyclic loading is applied to the test sample until failure, or until run away. Run away is defined as where the loading is below the fatigue limit, thus resulting in infinite cycle time. Note that the fatigue limit is an artificial limit introduced for practical reasons. Fatigue life increases exponentially as cyclic loading decreases, making it reasonable to assume infinite fatigue life with sufficiently low loading. This limit is usually set between 10^6 and 10^7 cycles.

To illustrate the fatigue life of a specific sample, a log-log straight line with the Stress-Cycles relationship, called a S-N curve, is commonly used. This line is often assumed to follow the Basquin equation

$$S_{NF} = A(N_f)^B \tag{2}$$

where S_{NF} is the fully reversed ($R = -1$) fatigue strength at N_f cycles, A is the coefficient that represents the value of S_{NF} at one cycle, and B is the slope of the S-N curve [23]. Even tho this is an approximation, it is often observed that materials follow this line quite accurately.

It is also worth noting that the mean stress during fatigue tests strongly influence the fatigue life obtained [23]. See figure 15. This is the reason why pulsating tension ($R = -1$) is often used, as it is considered the conservative choice.

16

Figure 15: Effect of mean stress on fatigue life. Figure from [23].
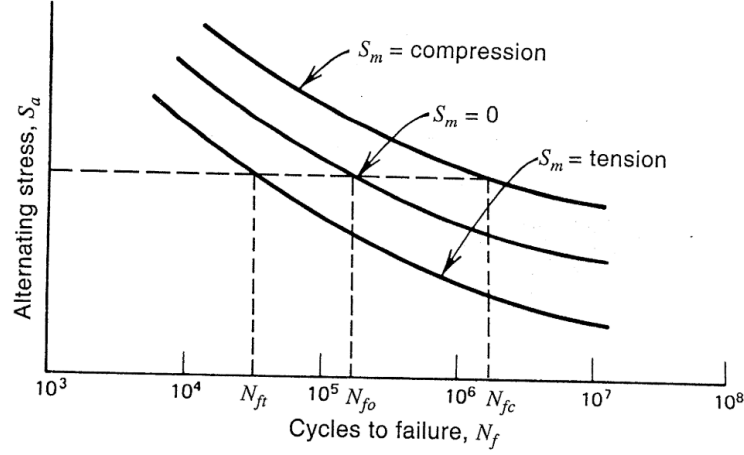
For a baseline for fatigue life of different alloys, a comparison is made in Table 4. Note that detailed production parameters have been left out for practical reasons. The table thus serves as a rough comparison, but should not be used for exact values.

Table 4: Fatigue strength overview of different alloys and production methods. All tests are axial with pulsating tension. Values from [24][14].

Alloy	Method	Fatigue Strength (MPa)
Al-Si-10Mg	SLM	77
Al-Si-10Mg	Cast	110
Ti-6Al-4V	SLM	243
Ti-6Al-4V	Cast	210

Surface finish is a vital parameter when talking about fatigue life, as cracks tend to start at the surface. The surface roughness can be viewed as micronotches. The more coarse the surface is, the more it behaves like notches, thus inducing stress concentrations. Surface treatment is therefore considered an important measure to improve fatigue life. It was for example reported an increase in fatigue life by S. Bagherifard et al. [6] of Al-Si-10Mg by 270% in shot peened samples, compared to as-build.

It is also worth mentioning that in the literature review of S. Beretta, S. Romano [25], it was reported fatigue limits of SLM produced Al-Si-10Mg from 57 MPa to 228 MPa, based on different print parameters. This highlights the need for study on this topic as well as showing that high fatigue strength is obtainable with the SLM technology.

2.3.1 Test methods

There are two different fatigue tests that are common when performing a fatigue test, namely *axial loading* and *rotating bending*. The former is defined by axial loading, resulting in uniformly distributed stress over the net cross section area. The latter is defined by applying a bending moment, thus causing the stress to distribute unevenly across the net cross section area, peaking at the surface, as illustrated in Figure 16. This makes rotating bending more sensitive to surface finish. Still, axial is considered the conservative choice. It was suggested

by Fuchs et al. [23] that a reduction of the rotating bending fatigue strength by 10-25% could be used to approximate axial fatigue strength.
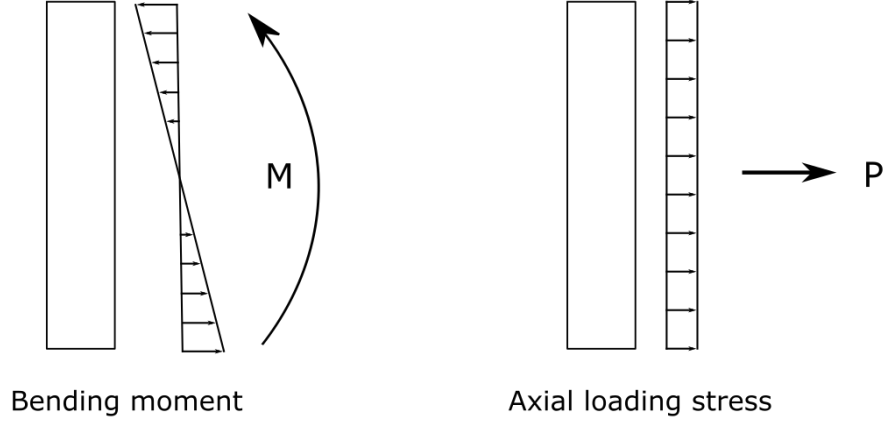

Figure 16: Illustration of stress distribution over the cross section from bending moment and from axial load. M is the applied momentum and P is the applied axial force.

2.4 Notch

Investigating notches in different materials is a way of learning how the material behaves with respect to geometrically induced stress concentration. Notch consideration is mainly used in the context of fatigue life, but is also relevant for static analysis. The first step in this evaluation is to determine the notch stress concentration factor K_t:

$$K_t = \frac{\sigma}{S} = \frac{\varepsilon}{e}, \quad \frac{\sigma}{\varepsilon} = const. = E \quad (3)$$

Where σ and ε represents local stress and strain, and S and e represents nominal stress and strain. Local stress is determined analytically, or by FEM analysis, based on the geometry of the notch [23]. The stress across the net section is distributed unevenly when a notch is present. The stress concentration

Figure 17: Stress distribution on notched geometry. Figure from [23].

factor is simply a measure of how much the peak stress will be, relative to an evenly distributed stress. Note that the sum of the stress over the net cross section will not change by the presence of a notch, only the distribution, as shown in Figure 17 [28].

K_t is sufficient to evaluate the notch with respect to static situations, but for fatigue consideration, some additional values is required to predict the material behaviour. Thus, an experimental value, the Fatigue Notch Factor K_f, is needed. K_f is defined by the smooth fatigue strength divided by the notched fatigue strength. By comparing these, it is possible to determine the materials notch sensitivity:
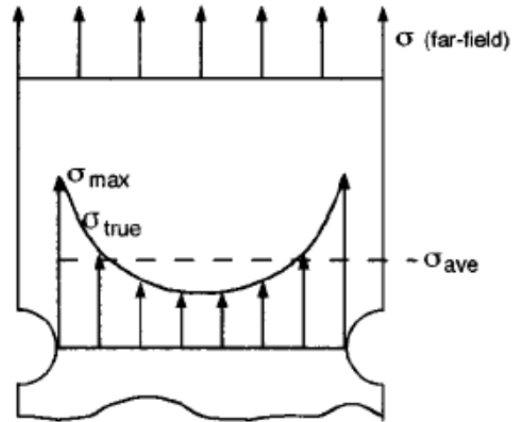
$$q = \frac{K_f - 1}{K_t - 1}, \quad R = -1 \tag{4}$$

Where q represents notch sensitivity and R is the stress ratio. This will be in the range of 0 to 1, where $q = 0$ indicates no notch sensitivity and $q = 1$ indicates full notch sensitivity.

2.5 Heat treatment

Heat treatment of metals is a common post processing application to enhance the mechanical properties of different alloys. The properties obtained are depending upon the heat treatment chosen, but is often related to either hardening or softening of the alloy.

An unintended heat treatment is not uncommon during production, as a result of a complex heat distribution and uneven cooling. Heat treatment can therefore also be utilized to minimize the effects of this, by making the material homogeneous, thus obtaining predictable characteristics.

2.5.1 Solution Heat Treatment

The process of solution heat treatment consists of two main steps. First, the part is heated to a high temperature. This allows the alloying elements to diffuse, making the alloy homogeneous. The ideal temperature is determined by the alloying elements and the corresponding phase diagram. The objective is to heat the alloy to a high enough temperature to dissolve the maximum amount of solute, while not causing melting in the grain boundary.

The time spent in this phase is highly dependent upon part geometry. A thin sheet can require less than a minute, while large inhomogeneous parts can require up to 20 hours [9].

Second, the part is quenched (Sec. 2.5.2), resulting in a supersaturated solid solution. This new distribution of alloying elements greatly increases ductility, while also decreasing strength.

2.5.2 Quenching

Quenching is the process of rapidly cooling the part from the heat treatment temperature, down to room temperature, thus obtaining a more fine microstructure than with furnace cooling[1] or by air cooling [9]. This is achieved by trapping the alloying phases in the solution before they have grown to their equilibrium grain size. This ensures a fine microstructure, which makes the material strong, but brittle.

To achieve this, the part is submerged in a quench medium. Common mediums are water, oil and brine, where the latter is water with a high concentration of salt. These provide different cooling rates, denoted by the Quench Severity (H). See Table 5 for example values. While submerged, the alloy undergoes three stages of cooling, namely (1) vapor blanket stage, (2) boiling stage and (3) liquid cooling stage. These are illustrated in Figure 18. The vapor blanket is maintained while the heat transfer from the part to the quench medium is high enough to evaporate the quenchant and maintain vapor phase. As soon as this is no longer the case, the boiling phase is initiated. This is where the cooling is the most rapid, as the quenchant is in contact with the part, but the heat transfer still induces phase change in the quench medium. The last stage is reached when the surface temperature of the part is equal to the boiling temperature of the quench medium. In this part of the

---

[1]Furnace cooling is the process of slowly turning down the temperature in the oven used for the heat treatment.

Table 5: Quench value for some quench mediums. Agitation refers to the relative movement between the quenched part and the quench medium. Table from [9].

	Quench Severity (H)		
Agitation	**Oil**	**Water**	**Brine**
None	0.25-0.30	0.9-1.0	2.0
Mild	0.30-0.35	1.0-1.1	2.0-2.2
Moderate	0.35-0.40	1.2-1.3	-
Good	0.40-0.50	1.4-1.5	-
Strong	0.50-0.80	1.6-2.0	-
Violent	0.80-1.1	4.0	5.0

quenching process, a too-rapid cooling could cause large amounts of residual stress. This favors oil, or another medium with high boiling temperature, as the temperature difference between quenchant and part core will be smaller during this phase.

2.5.3 Age Hardening

After solution treatment and quenching, some precipitation still occurs at room temperature. This will, over time, change the mechanical properties of the alloy. This natural aging greatly increases strength and elongation at yield and ultimate strength, while maintaining elongation at fracture. See Figure 19. For aluminum alloys, the process of solution heat treatment, quenching and natural aging is defined as the T4 temper. To enhance the effect of natural aging in some alloys, cold working can be utilized between quenching and aging. The cold working increases the dislocation density that serves as sites for nucleation of additional precipitate particles. Adding this step to the T4 temper gives the T3 temper [9].
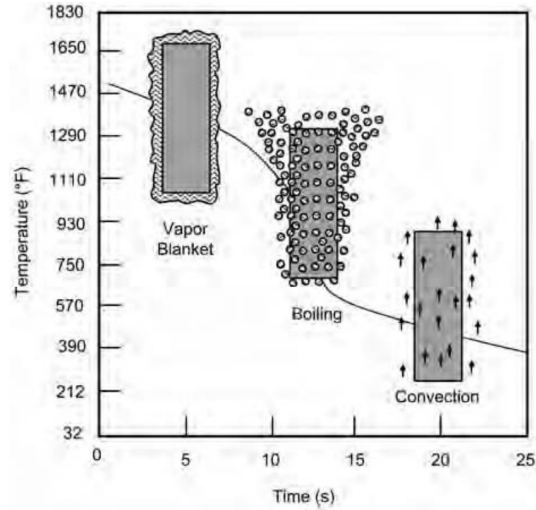

Figure 18: The three stages of quenching. Temperature values are example values for heat treatment of steel. Figure from [9].

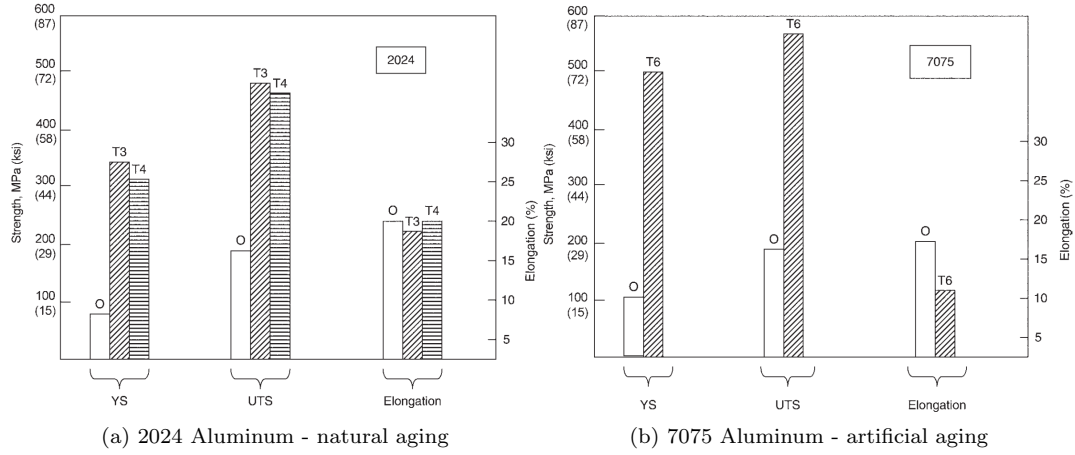(a) 2024 Aluminum - natural aging   (b) 7075 Aluminum - artificial aging

Figure 19: Effect of heat treatments on aluminum. YS, yield strength; UTS, ultimate tensile strength; O, solution heat treated and quenched. Figure from [9].

While some alloys reach stable characteristics from natural aging in a matter of days, other alloys takes years to finish the aging process. These undergo artificial aging to produce stable alloys. For aluminum alloys, solution heat treatment, quenching and artificially aging is known as the T6 temper. The artificial aging is conducted by heating the alloy to a low temperature (120-180°C) over a time period corresponding to the diffusion rate of the specific alloy, but is generally substantially longer than the solution heat treatment [9].

2.5.4   Hot Isostatic Pressing

Hot Isostatic Pressing (HIP) is a post processing method where the part is heated, typically above 70% of melting temperature, and subjected to a pressurized environment [5]. The pressure required is dependent upon the alloy, but is usually in the range of 100 to 200 MPa. This allows for gas pores to diffuse through the metal and leave the part entirely, thus reducing porosity. HIP has shown to improve mechanical properties independent of production method, but increasingly so for AM parts [11]. This makes HIP one of the favored post processing methods in Additive Manufacturing.

2.5.5   T6 Tempering of Al-Si-10Mg

In post processing Al-Si-10Mg, heat treatment after the T6 standard has showed to yield good results [6][19]. This is a two step method consisting of a solution treatment followed by artificial aging, with water quenching between and after the heated periods. In the former, the metal is heated to a temperature close to the eutectic melting point for a couple of hours. This makes the Si atoms precipitate from the supersaturated Al matrix, thus forming small Si particles. If the solution temperature is increased, the size of the Si particles will increase, but their number decrease. This results in lower yield and ultimate tensile strength, but increases elongation at fracture, as illustrated in Figure 20a. The artificial aging is characterized by lower temperature over a longer time period. In this process, diffused particles act like strengthening precipitates in the Al matrix. These particles are in the case of Al-Si-10Mg nanometer-scale Mg_2Si, and the size of these particles grow with increasing aging temperature and time [35].

(a) Only solution treatment　　　　(b) Heat treatment after T6 standard
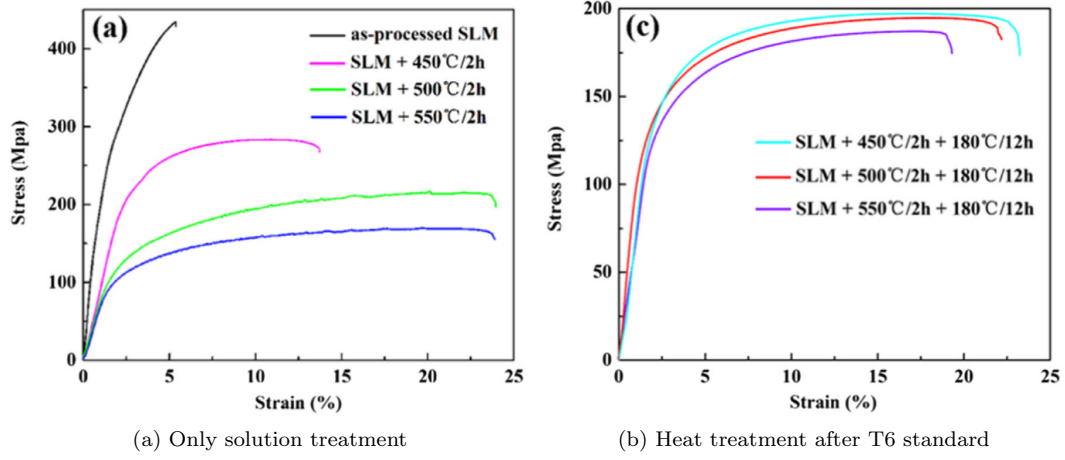
Figure 20: Heat treated Al-Si-10Mg. Graphs from [19].

As mentioned in Section 2.1 and illustrated in Figure 1, the eutectic solubility of Si in Al is about 12.2 wt.%. The maximum equilibrium solid solubility is however 1.59 wt.% at the eutectic temperature [4]. By utilizing water quenching after the solution heat treatment, the Si particles have a very limited time window in which to diffuse further from the Al, thus trapping it in place.

The heat treatment has a significant influence on the mechanical properties of Al-Si-10Mg, as is expected of aluminum alloys (Figure 19). It was reported by W. Li et al. [19] that solution heat treatment alone could reduce the tensile strength to 38.7% of As-Build value, while increasing fracture strain by 447% (see Fig. 20a). Heat treatment is therefore considered a vital parameter to optimize and understand Al-Si-10Mg.

3 Fatigue testing of SLM produced Al-Si-10Mg

As discussed in 2.2, additive manufacturing is rapidly being implemented in industry, with new materials and new areas of use being added to the AM application list all the time. However, fatigue life of notched AM metals has only recently been investigated in literature and these properties remain undiscovered for many commonly used alloys. Characterizing fatigue behaviour in notched specimens is therefore considered by the author to be a vital step towards allowing engineers to further utilize this technology. The testing done in this paper aims to contribute to the development of these characteristics, thus helping future engineers in their design process.

Table 6: Chemical composition of Al-Si-10Mg powder provided by the supplier.

Element	Al	Si	Fe	Cu	Mn	Mg	Zn	Ti
Minimum	Balance	9.0	-	-	-	0.2	-	-
Actual	Balance	9.8	0.24	<0.005	<0.005	0.44	<0.002	<0.01
Maximum	Balance	11	0.55	0.05	0.45	0.45	0.1	0.15

3.1 Experimantal setup

3.1.1 Fatigue testing

The specimens were tested on a MTS Landmark 50 kN machine with axial loading and a frequency of 10 Hz, and some at a Instron E10000 with the same loading, but at 40-50 Hz. The tests were preformed with a stress ratio of $R = 0$ and run out limit was set to 2×10^6 for practical reasons.

3.1.2 Microscopy

The microstructure was examined using Scanning Electron Microscope (SEM) and Optical Microscope (OM), while the fracture surfaces were imaged with the SEM only.

In preparation of the fracture surface imaging, the samples were thoroughly washed in ethanol, using an ultrasonic bath for about 3-5 minutes. This removed any dust particles from the surface, thus allowing for clear imaging. Any dust particle on the fracture surface would accumulate negative charge as it is bombarded with electrons in the SEM, which would leave a black spot in the images, as the negatively charged dust particle would repel the electrons from the SEM.

3.1.3 Fracture surface analysis

The images from the SEM were imported to a vector based drawing software (Inkscape), where the fracture surface were analyzed with respect to defects at the geometry surface. Four different measurements were made to allow for two main defect tracking methods, namely gas inclusions and area loss.
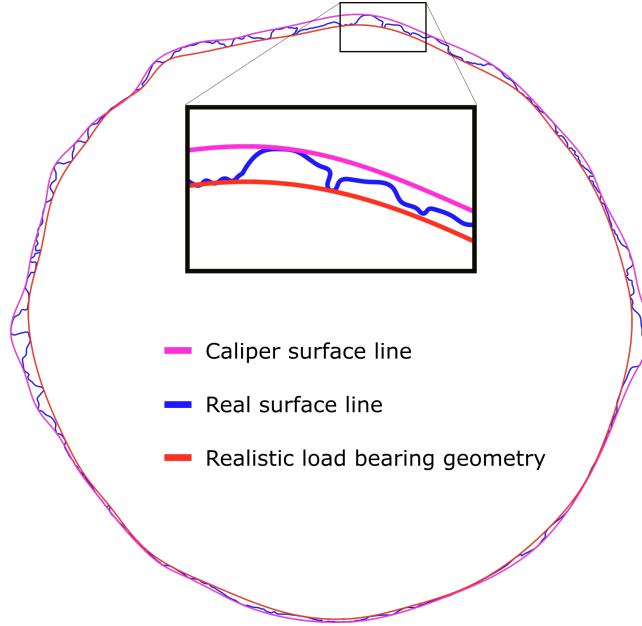
Figure 21: Example of surface measurements.

Gas inclusions. These were limited to internal gas inclusions who satisfy the conditions $L < 4d$, where L is the distance from the defect to the geometry surface, and d is the diameter of the defect. This is in accordance with the conclusions of Biswal et al. [8], as the findings in their work showed that any gas inclusion within these limits were influenced by a surface effect. Further, any subsurface gas inclusion where $d < 15\mu m$ were excluded. See Figure 22. These were evaluated in the fatigue crack growth zone only.

Surface area loss. Since there is no obviously preferred defect measurement method for fracture surfaces observed in literature, an experimental approach were conducted to evaluate the samples in this regard. The observed *Real surface line (R)* were initially traced, and the *Caliper surface line (C)* and *Realistic Load bearing geometry (RL)* were drawn based on this. The area difference between these were used as a measurement of defects, including both surface roughness and lack of fusion. Note that the surface estimations were done by hand. This induces some degree of uncertainty, but is assumed to be accurate enough for empirical analysis. See Figure 21.

The cross section area were also adjusted based on the listed lines. Here, the applied load were spread onto the observed area, thus creating a more realistic stress level. The adjustments made were for *Real Area (RA)*, *Load bearing Area (LA)* and *Theoretical Area (TA)*. These were evaluated in conjunction with the surface roughness measurements, as shown in Table 7. It is expected from literature that LA will be the most accurate area adjustment [21].

However, this approach includes evaluation of the whole fracture surface, thus the ductile part is also contributing to the area loss. The ductile part is known to be the final fracture area, and can not contribute to the crack propagation, hence it is reasonable to exclude this from the defect analysis. Some additional analysis were therefore carried out, with respect to the *Fatigue Crack growth zone (FC)* only. The separation were done quite coarsely, splitting the lines radially from the centre of area of the real surface line (Figure 21) to obtain the

24
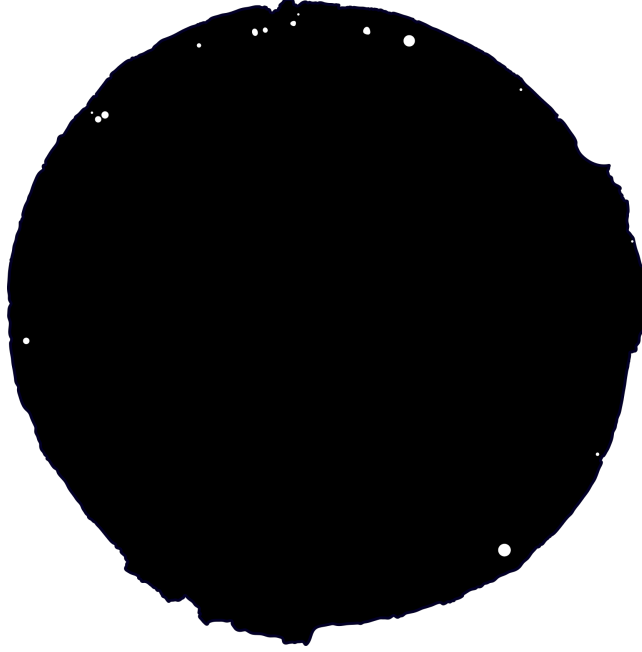
Figure 22: Gas inclusions observed in example fracture surface.

fatigue area. This is shown in Figure 24. Since the measurements based on this division only concerns the surface area, this method is considered adequate.

Table 7: Matrix showing the empirical evaluation methods of surface roughness measurements and load bearing measurements. A1, A2 etc. denotes the corresponding S-N diagram.

Area / Defect	None	C-R	C-L	R-L	(C-R)FC	(C-L)FC	(R-L)FC
TA	A1	B1	C1	D1	E1	F1	G1
RA	A2	B2	C2	D2	E2	F2	G2
LA	A3	B3	C3	D3	E3	F3	G3

A similar evaluation were done with respect to the gas inclusions, where the area of the gas inclusion in the fracture surface served as the *area loss* parameter. These graphs were given names after the same fashion as the surface area loss graphs. Thus, H1 is the S-N graph with gas inclusions as the defect measurement and theoretical area as load distribution area, H2 uses *Real Area* while H3 uses *Load bearing Area*.

The S-N diagrams were created as bubble diagrams, where the area loss (included defects) were implemented as the size of the bubbles. If the bubbles formed separate lines, the measurement method would be considered sufficient to predict better-than-normal fatigue life for the specimen. See Figure 23. Further, the amount of scatter was used to determine the quality of the measurements, where lower scatter indicates a better prediction.
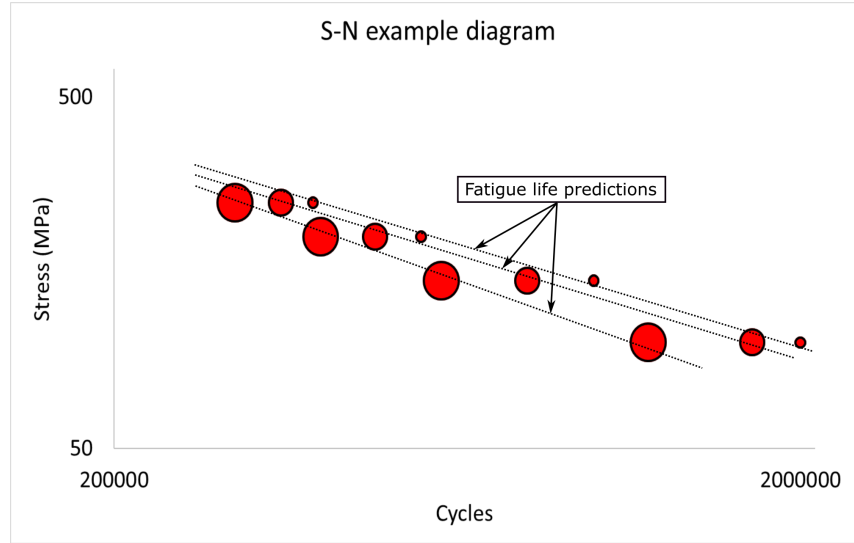
Figure 23: Schematic of desired graph obtained from defect and surface roughness measurements of the test series.
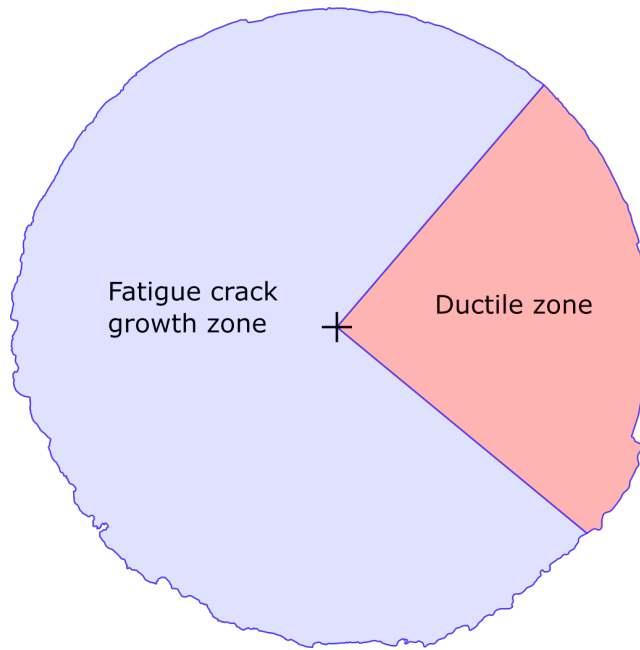
Figure 24: Measurements of fracture surface with respect to fatigue crack growth zone.

3.2   Samples

SLM printed Al-Si-10Mg alloy is the subject of testing in this paper. The samples were produced identically to the ones used in [6], from the same supplier, thus the same material characteristics are attributed to the samples used in these experiments. See table 6. The samples were tested both in as-build condition and with heat treatment after the T6 standard

(2.5).

3.2.1 U-notch

These samples have dimensions as shown in Figure 25. The notch is characterized as a u-shaped notch, with r = 0.5, $\frac{D}{d} = 2$ and $\frac{r}{d} = 0.1$, where r is the notch radius, D is the sample diameter and d is the diameter at the notch. To determine stress concentration factor K_t analytically, an online calculator based on Petersons calculations is utilized [2]. This gives $K_t = 2.60$ for the specimen.
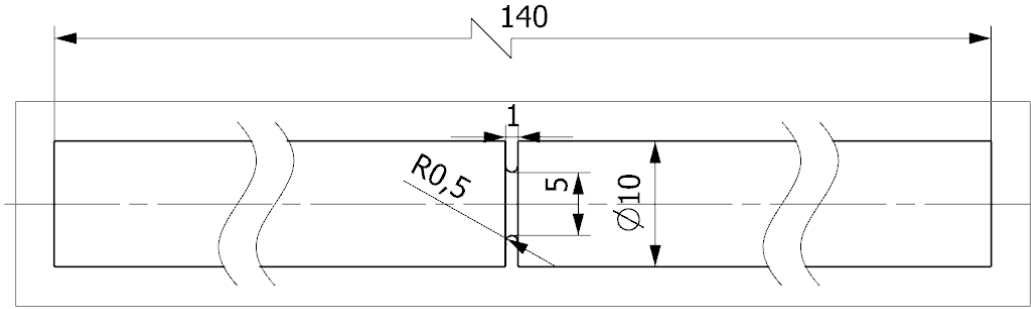
Figure 25: Geometry of notched sample used in fatigue tests. Units in mm.

To get some more data on the stress concentration factor, a Finite Element Model (FEM) based evaluation was carried out in Abaqus. This simulation was done by creating an axisymmetric 2D representation of the sample. A force was applied to the top surface, thus representing the actual test conditions. To determine the refinement of the mesh, a mesh convergence test was preformed. The convergence condition was set to 0.1%, meaning that the mesh is assumed to give accurate results for the stress concentration when

$$\left| \frac{K_{t,n} - K_{t,n-1}}{K_{t,n}} \right| \leq 0.001$$

where n is the iteration number with decreasing mesh size. The mesh convergence is displayed in Figure 26.
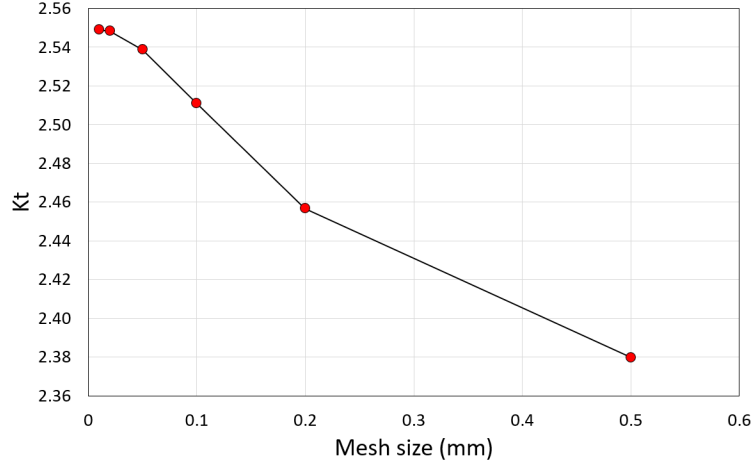
Figure 26: Variation in simulated value of K_t with respect to element size at notch surface.

Analyzing the mesh convergence and calculating the change in K_t, the values in Table 8 were obtained. It is observed that a very fine mesh of 0.01 mm (See figure 27a and 27b) is required to achieve satisfactory convergence. This gives $K_t = 2.549$, which is fairly similar to the value obtained from the online calculator. However, it is assumed that the FEM method is more accurate, hence the value of 2.549 for the stress concentration factor will be used from here on.

(a) Mesh topology of model used to determine K_t.

(b) Mesh resolution of 0.01 mm at notch surface.
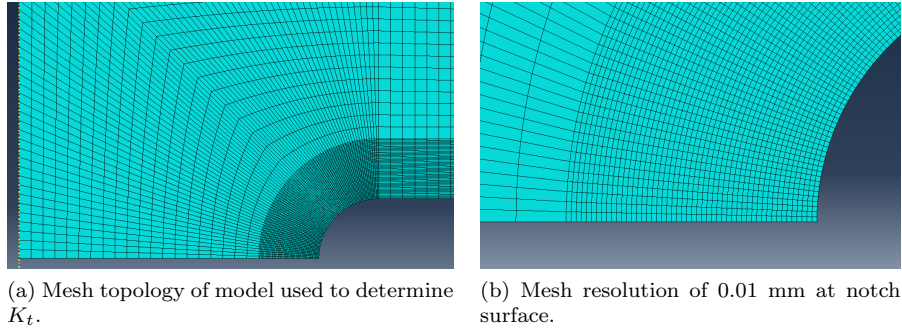
Figure 27: Mesh refinement for notch analysis.

To establish an understanding of the stress distribution over the cross section surface at the notch, the stress concentration was measured in the FEM analysis. The measurement was done from the centre of the notch surface, where the stress is highest, to the centre axis of the sample. The results are displayed in Figure 28. This distribution does to a large degree follow the expected curve from theory, as shown in Figure 17. Note that this stress is evenly spread

Table 8: Change in K_t with respect to mesh size.

Mesh size (mm)	K_t	Change (%)
0.50	2.380	-
0.20	2.457	3.13
0.10	2.511	2.16
0.05	2.539	1.09
0.02	2.548	0.37
0.01	2.549	0.03

in the angular direction. This means that the surface of the U-notch experience the highest amount of stress, all around the sample. This is shown in the visual representation of the analysis in Figure 29.
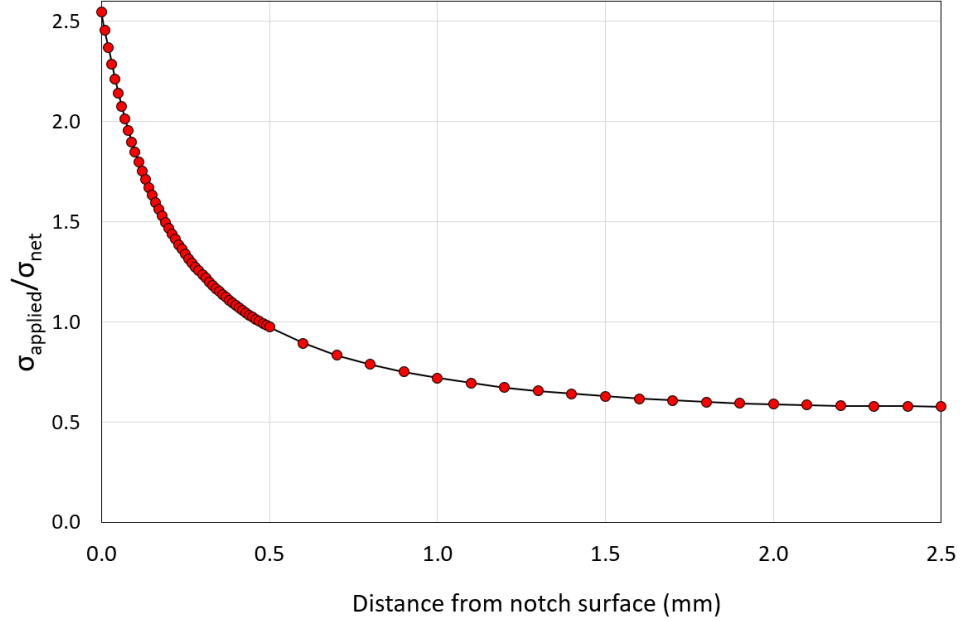
Figure 28: Relative stress distribution over the cross section area at the notch.
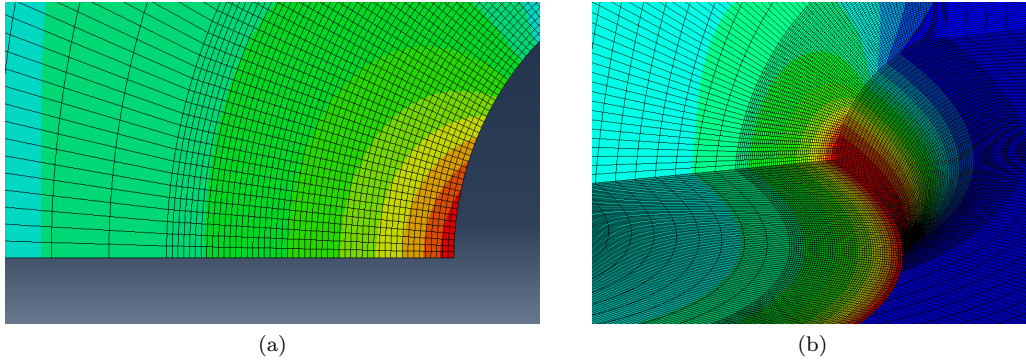
Figure 29: Visualization of stress distribution at the notch.

For values of surface roughness, the measured average roughness (R_a) was found to be 9 μm for both as-build and heat treated samples by S. Bagherifard et al. [6], and will also be the same for the samples used here. The porosity was measured to 0.2% for as-build and 0.4% for heat treated samples.

3.2.2 Smooth

To obtain reference values for the material and production method used, fatigue tests on smooth samples were preformed. These are designed so that the stress concentration factor

$K_t \simeq 1$. See Figure 30.
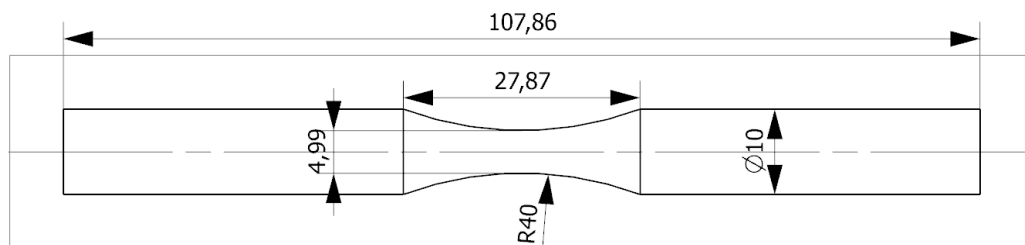
Figure 30: Geometry of smooth sample used in fatigue tests. Units in mm.

This design for uniform stress distribution were examined by FEA, in the same way as the notched geometry. It was found that $K_t = 1.025$, which is considered acceptable for smooth samples. Total relative stress distribution over the cross section is given in Figure 32.
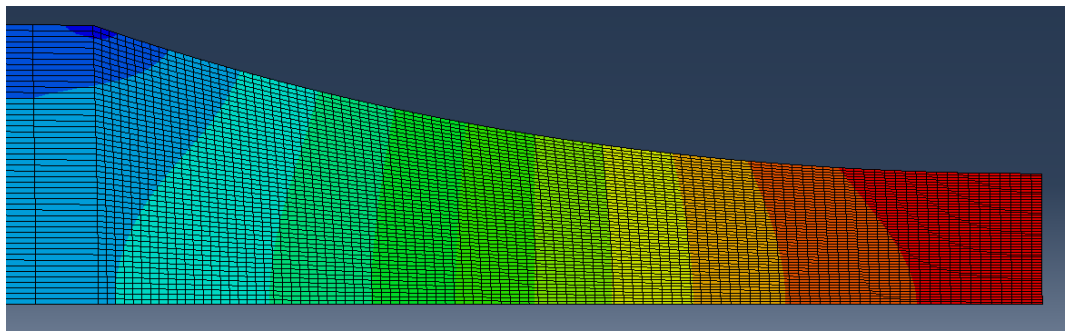
Figure 31: Mesh and stress distribution visualization on smooth sample.
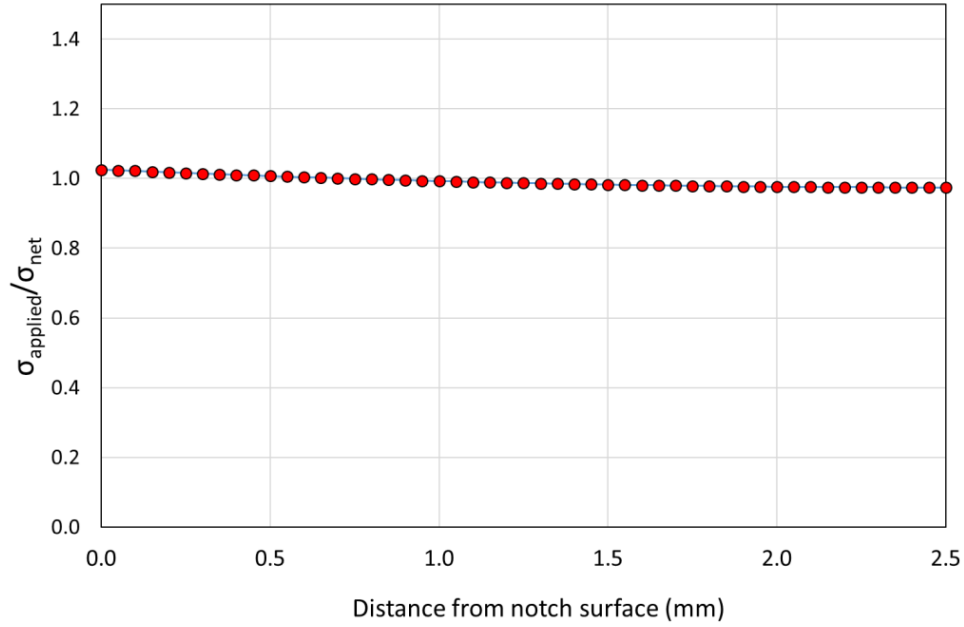
Figure 32: Relative stress distribution over the cross section on the smooth geometry.

3.3   Results

In this section, the results from the experiments will be presented. These are divided into *Topology*, *Fractography* and *Fatigue*, where the first is connected to dimmensional accuracy, the second concerns the defect identification and surface analysis, and the third is focused on fatigue life predictions based on the tests preformed. Additionally, a fourth result evaluation is conducted, making an attempt to combine the first three. This subsection is called *Defect Dependent Fatigue Life*.

3.3.1   Topology

To examine the degree of dimensional accuracy from production, the cross section of a notched heat treated sample were subject to investigation with OM, as displayed in Figure 33. It was discovered that the obtained geometry differed quite noticeably from the theoretical geometry, thus making the calculated value for stress concentration (K_t) somewhat more uncertain. However, it is worth noting that only one samples were subject to dimensional analysis with OM, thus no trends in topology deviation could be determined.
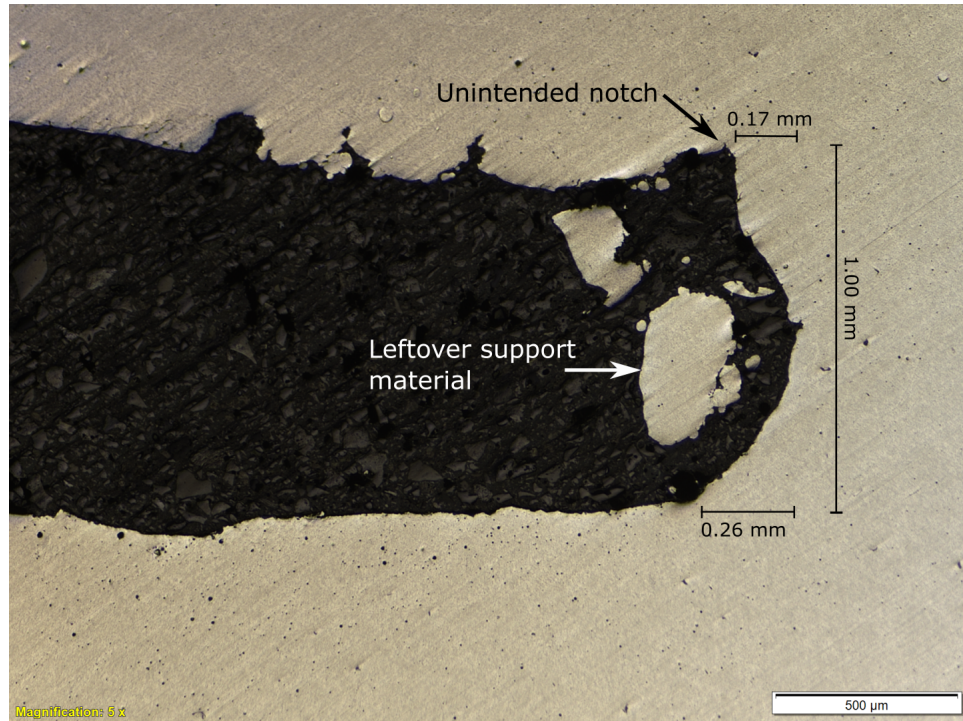
Figure 33: Actual dimensions of notched sample.

3.3.2 Fractography

Examining an example fracture surface from the series by SEM, seen in Figure 34, it is observed that the material is quite uniformly melted with close to no internal defects. This was, quite remarkably, true for most of the samples in both the heat treated and the as-build series of the notched and smooth samples. Further, it is observed that the as-build fracture surfaces has more noticeable scanning pattern. This was true for all samples, not only the example surfaces presented here.

(a) Smooth, as-build. (b) Smooth, heat treated.

(c) Notched, as-build. (d) Notched, heat treated.
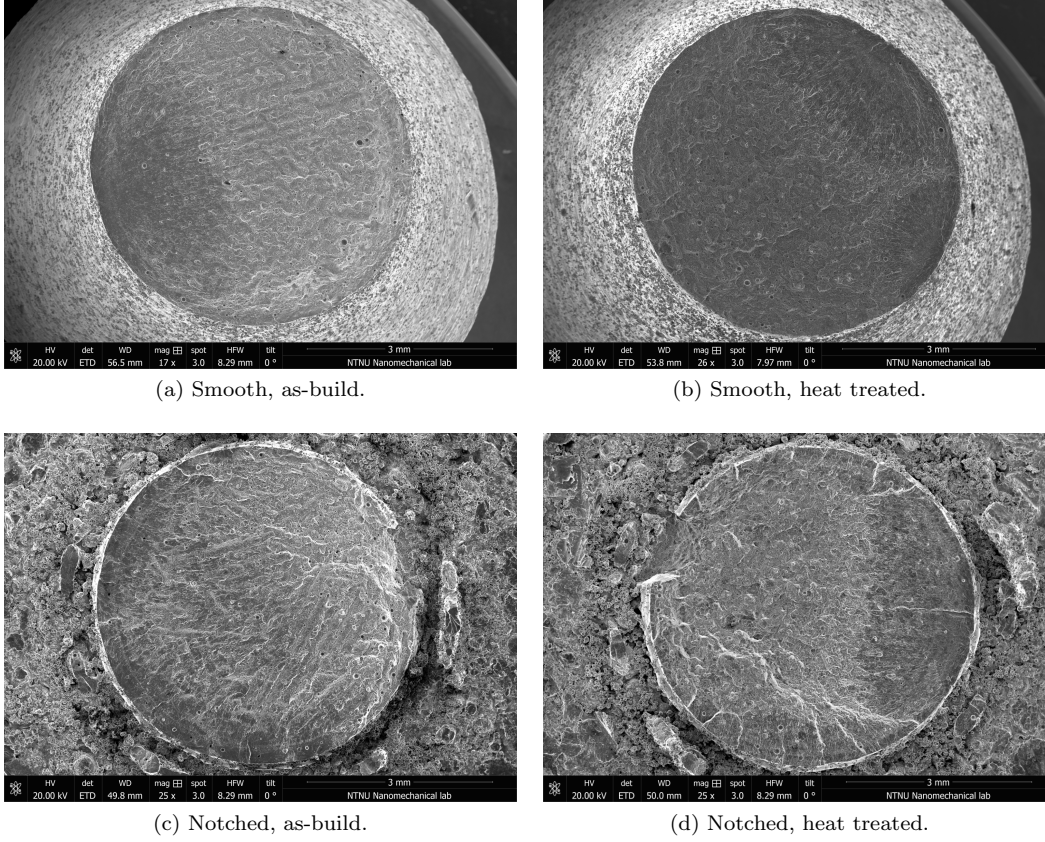
Figure 34: Example fracture surfaces from all 4 series.

Fatigue cracks were observed to initiate mainly from surface defects, as shown in 36a, which can also be characterized as surface roughness. In the notched case, multiple crack initiations usually occurred along the surface (Figure 36b). As they propagated, they eventually combined, creating a multilayered topography with ductile fracture combining the plateaus. On rare occasions, the crack initiations were identified as lack of fusion, as shown in Figure 36c and 36d. Further, some of the cracks initiated from seemingly inconsequential surface defects. In some of these instances, gas inclusions were located in close proximity to the initiation site, thus indicating that the increase in local stress around the void contributed to the crack initiation. Examples of this is provided in Figure 36e and 36f. The thin white lines appearing in all the images showcased in Figure 36 indicates the fatigue crack growth direction. Some samples also appeared to have failed not from the designed notch root, but from the base of the notch topology. An example of this is provided in Figure 35.

In the smooth series however, there were mostly one main defect from which the crack propagated. This resulted in a flatter surface without the layered characteristics observed in the notched case.

| ⚛ | HV | det | WD | mag ⊞ | spot | HFW | tilt | ├─────── 3 mm ───────┤ |
| | 20.00 kV | ETD | 49.2 mm | 25 x | 3.0 | 8.29 mm | 0 ° | NTNU Nanomechanical lab |
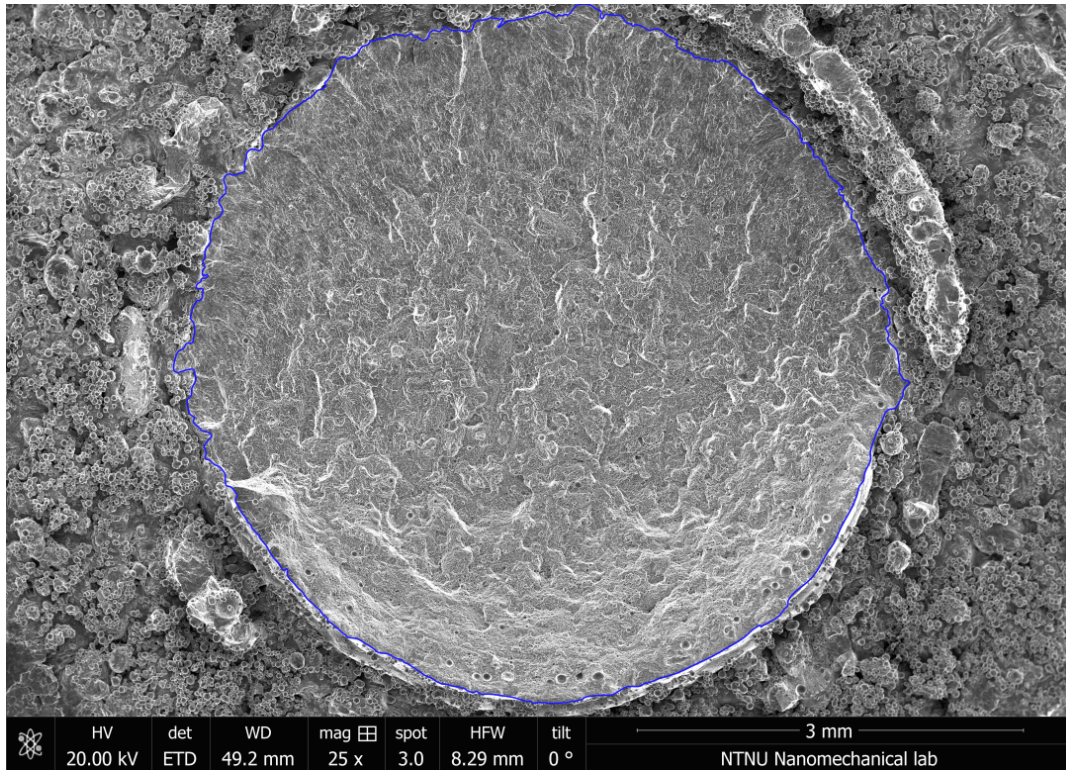
Figure 35: Example of sample with apparent crack initiation from the base of the notch. The blue line is the geometry surface line.
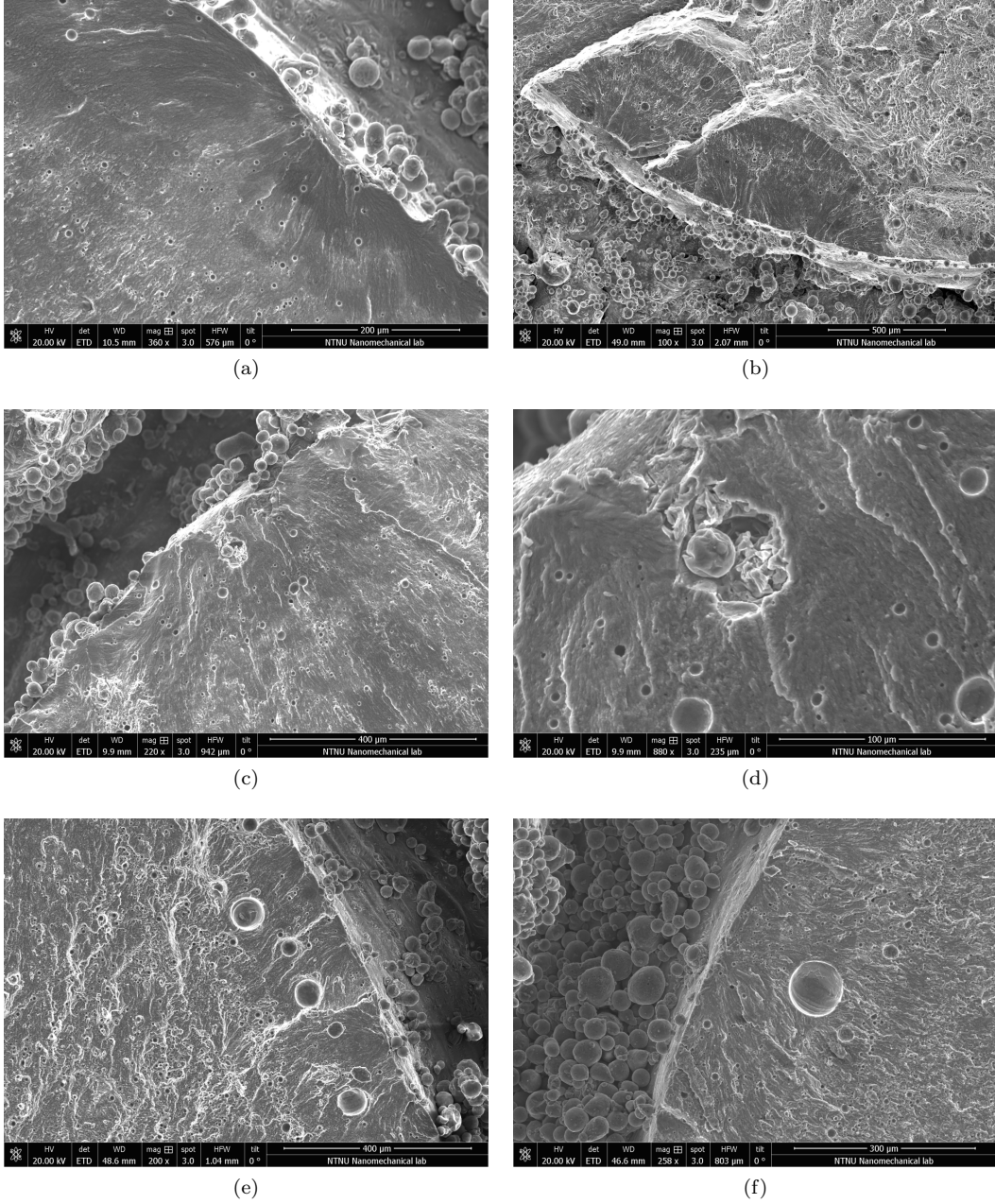
Figure 36: Crack initiations in notched heat treated test series.

Analyzing the fracture surfaces, it was observed that the cross section area was larger than the designed geometry, thus creating a discrepancy between the theoretical area and the actual area. The average area deviation deduced from the surface lines illustrated in Figure 21 are shown in Table 9.

Table 9: Fracture surface area analysis table. RA = Real Area, LA = Load bearing Area, S = Standard deviation. Values represented as % of Theoretical Area at $\pi \times (2.5mm)^2 = 19.635mm^2$.

Series	Avg. RA	Avg. LA	S_{ra}	S_{la}
Notched, HT	110.11	108.32	2.80	2.09
Notched, AB	110.22	108.79	3.27	2.51
Smooth, HT	100.64	99.96	4.01	3.95
Smooth, AB	107.35	106.80	3.62	3.59

The zones identified in the fracture surfaces can be split into three different stages of fracture, as shown in Figure 37 and 38. These can be recognized as *fatigue crack initiation*, *fatigue crack growth* and *final fracture*. The first of the three is characterized by a flat and dark area. This is due to the slow crack growth, shown by short striation in this region (Figure 39). The fatigue crack growth zone is recognized by a somewhat flat area, but with more noticeable lines caused by a small degree of ductile fracture, as well as longer striation. The final fracture is identified by exclusively ductile fracture.
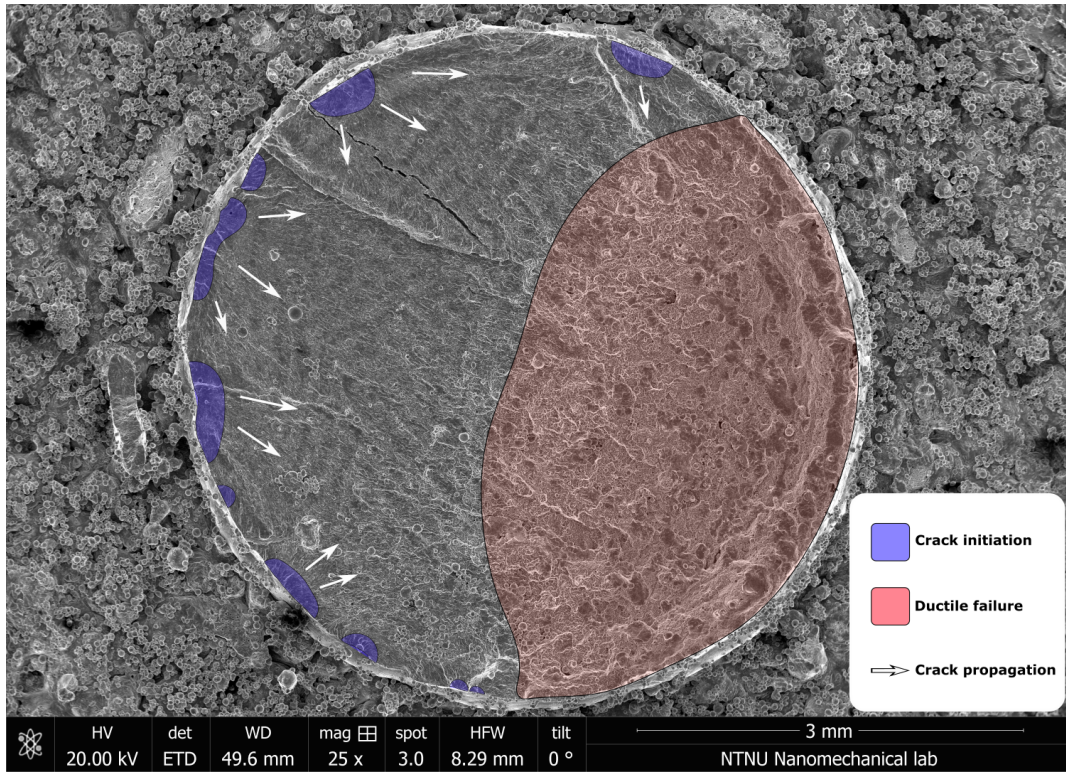
Figure 37: Fatigue crack growth zones. Notched, heat treated sample.
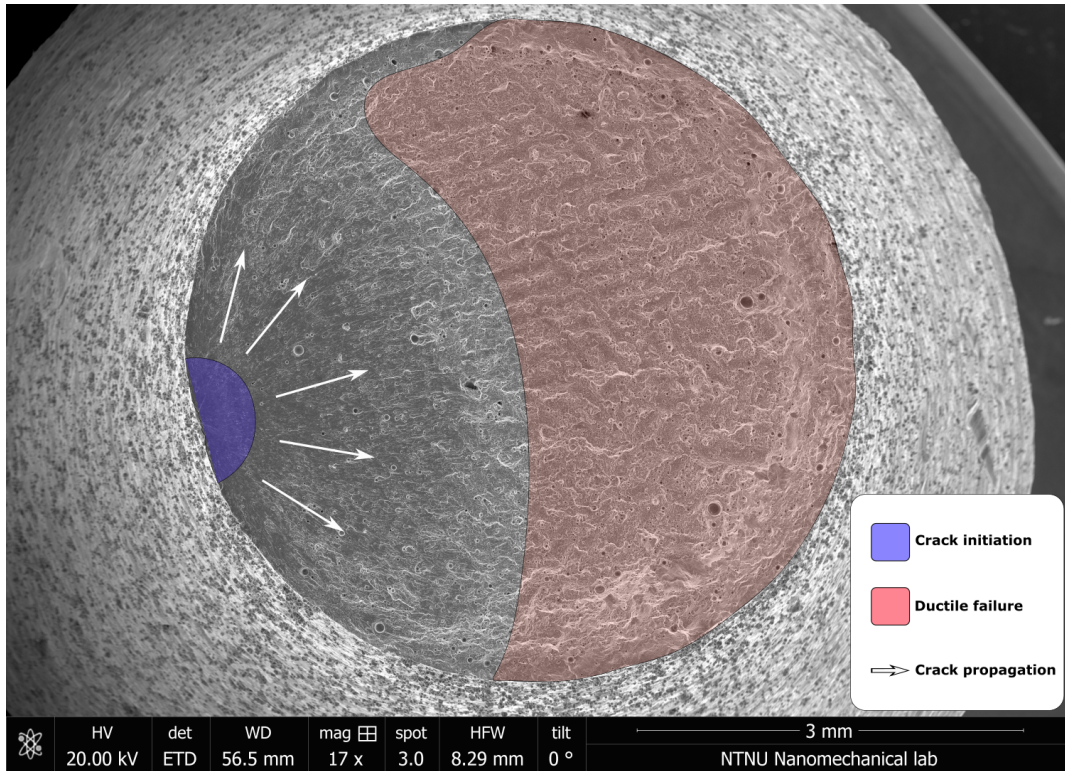
Figure 38: Fatigue crack growth zones. Smooth, as-build sample.

The striation in a given region of the fatigue crack propagation is a measure of the speed of the crack growth. The distance between two striation lines represents one cycle during the fatigue test, thus creating a linear relationship between striation density and crack propagation. This is shown in Figure 39. Here, any striation lines are hard to observe at all at the crack initiation, while an increase in the distance between lines are observed closer to the ductile area, compared to the early stages of crack propagation.

(a) Crack initiation.

(b) Early stage crack propagation.

(c) Late stage crack propagation.

(d) Final fracture.
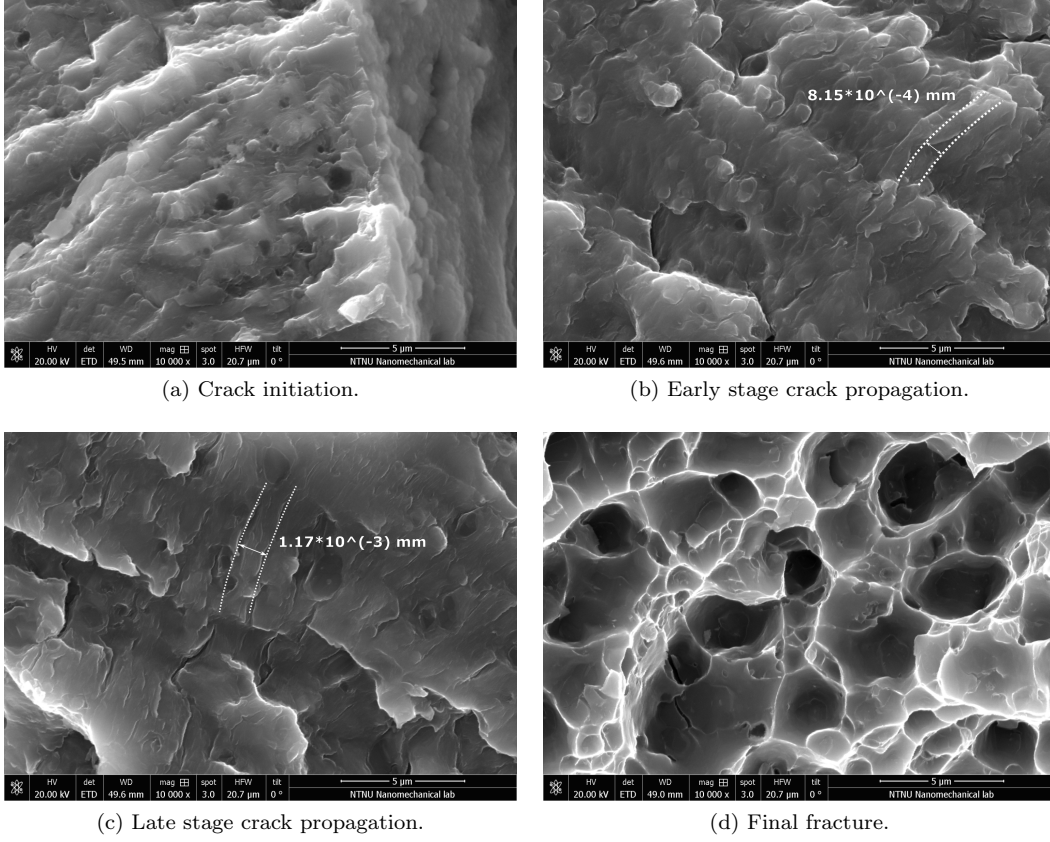
Figure 39: Striation from notched heat treated sample.

3.3.3 Fatigue results

Results obtained from fatigue testing of the samples are presented in Figure 40, 41, 42 and 43, as well as summarized in Table 10. It is observed that the data follow the expected log S - log N line to a satisfactory degree, and that the low scatter index indicates accurate fatigue life predictions.

Table 10: Results from fatigue testing of SLM Al-Si-10Mg. σ_x represents the life expectancy of x% of the samples. T_σ represents scatter index and k is the inverse of the slope.

Sample Series	σ_{90} (MPa)	σ_{50} (Mpa)	σ_{10} (MPa)	T_σ	k
Notched, AB	37.73	42.29	48.78	1.293	4.00
Notched, HT	53.64	64.38	77.27	1.441	4.84
Smooth, AB	65.17	70.32	75.88	1.164	4.11
Smooth, HT	96.09	110.41	126.88	1.320	5.12
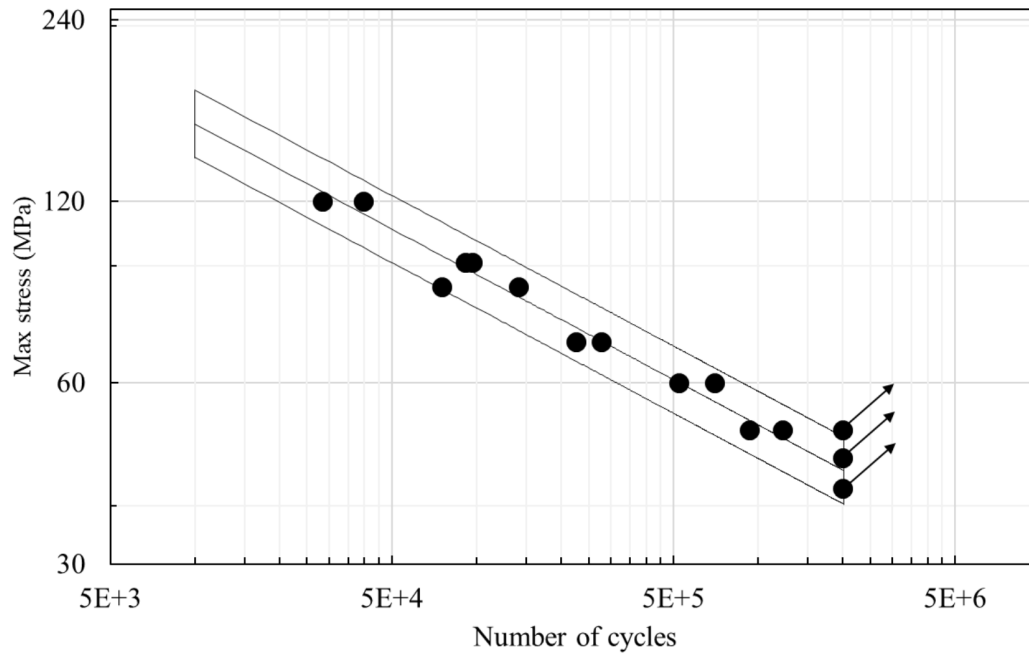
Figure 40: S-N curve of as-build U-notched Al-Si-10Mg, with confidence bands at 90% and 10%. Tests stopped at 2×10^6 cycles are marked with an arrow.
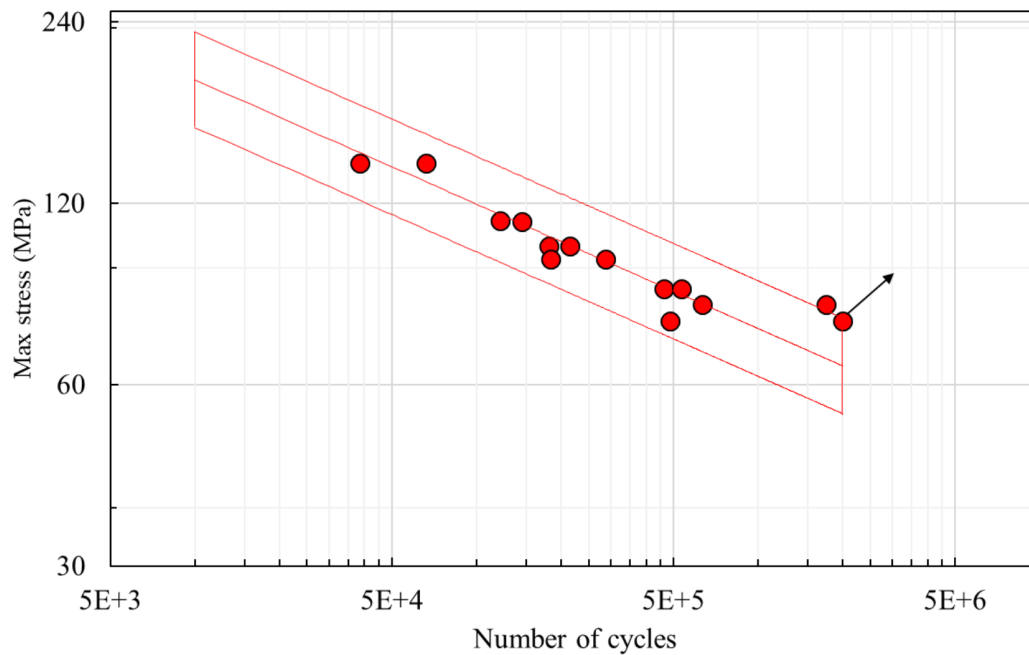
Figure 41: S-N curve of heat treated U-notched Al-Si-10Mg, with confidence bands at 90% and 10%. Tests stopped at 2×10^6 cycles are marked with an arrow.
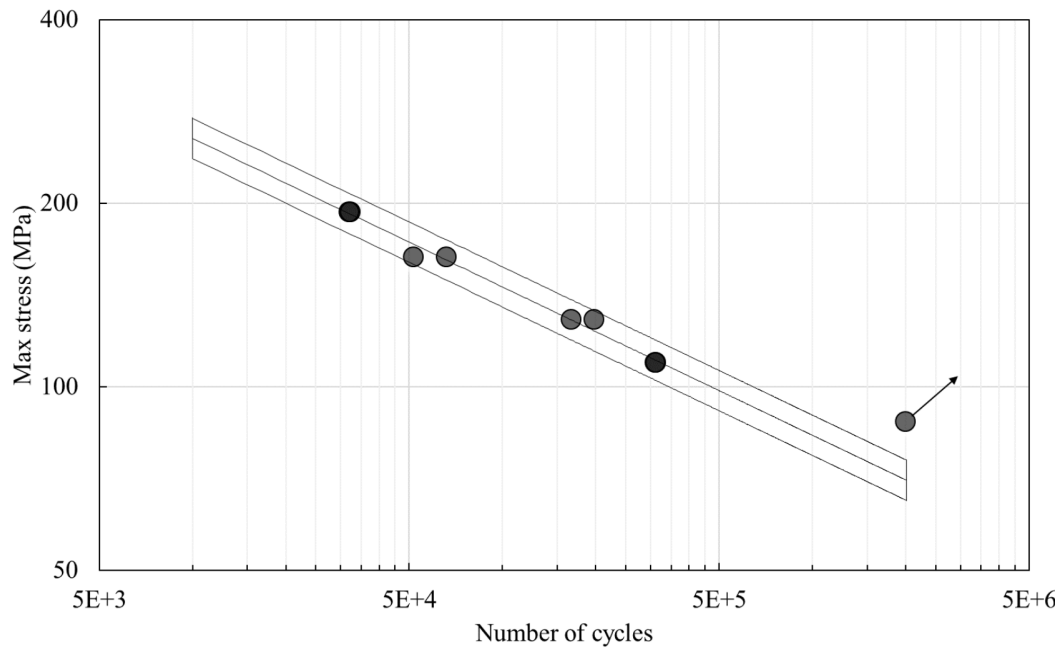
Figure 42: S-N curve of as-build smooth Al-Si-10Mg, with confidence bands at 90% and 10%. Tests stopped at 2×10^6 cycles are marked with an arrow.
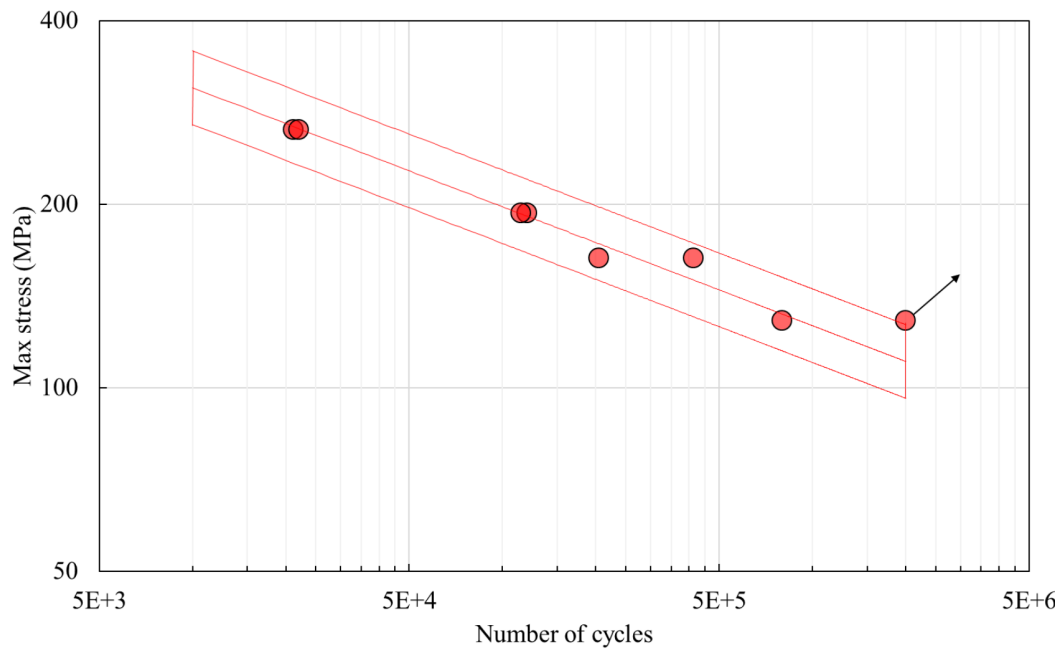
Figure 43: S-N curve of heat treated smooth Al-Si-10Mg, with confidence bands at 90% and 10%. Tests stopped at 2×10^6 cycles are marked with an arrow.

The scatter index T_σ in Table 10 refers to the relationship between the 90 percentile and the 10 percentile fatigue strength levels, thus giving $T_\sigma = \frac{\sigma_{10}}{\sigma_{90}}$. Scatter index is simply put a measurement of the predictability of the fatigue strength of the material. The low scatter index in the data obtained here therefore indicates good fatigue prediction accuracy.

To further parametrize the behavior, the exponential slope B in the Basquin equation (eq. 2) is calculated. The value for A is substituted with the ultimate strength of the material, giving $A_{HT} = 265MPa$ and $A_{AB} = 393MPa$ [6]. The evaluation point is chosen to be at 2 million cycles.

$$B = \frac{log(\frac{S_{NF}}{A})}{log(N_f)} \rightarrow B_{HT} = -0.095, \quad B_{AB} = -0.157$$

3.3.4 Defect dependent fatigue life

Using the methods described in Section 3.1.3, the fatigue data of the heat treated series were evaluated with respect to defects. The experimental graphs suggested in Table 7 are split into two separate S-N curves, where *min* denotes the portion of samples with small defects and *max* denotes large defects, relatively. The graphs were split at the sample median, or close to the median, where there was a natural division in defect size. These results are presented in Table 11. Note that the F- and G-series are identical in their predictions. This is because the samples with large defects after the (C-L)FC measurement are the exact same samples with large defects after the (R-L)FC measurement (Table 7). This is not that surprising, since the graph has a limited amount of data points, and the former includes the latter. Further, it is worth mentioning that the A1 graph represents the S-N curve of the whole heat treated series, also displayed in Table 10.

Table 11: Data from empirical analysis of S-N diagrams with respect to defects based on surface area loss.

Graph	σ_{50} (Mpa)	T_σ	k	Defect range (mm^2)	Data points
A1	64.38	1.441	4.84	-	13
A2	57.88	1.529	4.73	-	13
A3	59.21	1.492	4.80	-	13
$B1_{min}$	68.79	1.723	5.36	0.15 - 0.30	7
$B1_{max}$	57.91	1.510	4.06	0.36 - 0.52	6
$B2_{min}$	64.14	1.688	5.47	0.15 - 0.30	7
$B2_{max}$	57.91	1.510	4.06	0.36 - 0.52	6
$B3_{min}$	64.98	1.659	5.50	0.15 - 0.30	7
$B3_{max}$	53.08	1.654	4.12	0.36 - 0.52	6
$C1_{min}$	69.16	1.978	5.39	0.33 - 0.54	6
$C1_{max}$	58.07	1.403	4.04	0.61 - 1.10	7
$C2_{min}$	64.71	1.910	5.52	0.33 - 0.54	6
$C2_{max}$	52.11	1.560	4.08	0.61 - 1.10	7
$C3_{min}$	65.43	1.878	5.53	0.33 - 0.54	6
$C3_{max}$	53.02	1.540	4.04	0.61 - 1.10	7
$D1_{min}$	68.69	1.726	5.34	0.15 - 0.29	7
$D1_{max}$	55.16	1.422	3.76	0.37 - 0.65	6
$D2_{min}$	64.23	1.681	5.46	0.15 - 0.29	7
$D2_{max}$	49.30	1.516	3.80	0.37 - 0.65	6
$D3_{min}$	65.00	1.656	5.48	0.15 - 0.29	7
$D3_{max}$	50.11	1.521	3.76	0.37 - 0.65	6
$E1_{min}$	68.79	1.723	5.36	0.08 - 0.17	7
$E1_{max}$	57.91	1.510	4.06	0.23 - 0.42	6
$E2_{min}$	64.14	1.688	5.47	0.08 - 0.17	7
$E2_{max}$	52.24	1.669	4.18	0.23 - 0.42	6
$E3_{min}$	64.98	1.659	5.50	0.08 - 0.17	7
$E3_{max}$	53.08	1.654	4.12	0.23 - 0.42	6
$F1_{min}$	68.44	1.584	5.32	0.15 - 0.40	8
$F1_{max}$	54.67	1.544	3.76	0.73 - 0.90	5
$F2_{min}$	63.83	1.557	5.43	0.15 - 0.40	8
$F2_{max}$	49.29	1.512	3.91	0.73 - 0.90	5
$F3_{min}$	64.69	1.533	5.46	0.15 - 0.40	8
$F3_{max}$	49.98	1.561	3.84	0.73 - 0.90	5
$G1_{min}$	68.44	1.584	5.32	0.08 - 0.21	8
$G1_{max}$	54.67	1.544	3.76	0.36 - 0.52	5
$G2_{min}$	63.83	1.557	5.43	0.08 - 0.21	8
$G2_{max}$	49.29	1.512	3.91	0.36 - 0.52	5
$G3_{min}$	64.69	1.533	5.46	0.08 - 0.21	8
$G3_{max}$	49.98	1.561	3.84	0.36 - 0.52	5

It is observed from the S-N data obtained in Table 11 that the predictability, dependent upon the scatter (T_σ), was on average somewhat lower than the full series. Still, the scatter index of every independent evaluation is below 2.0, thus indicating that the values are quite reliable. The most reliable evaluation were found to be the *F2* and *G2* graphs, with a scatter index of 1.557 for the *min* part and 1.512 for the *max* part. It was generally observed that the *max* part, containing the large defects, had lower scatter index and lower k value.

Using *F2* as the basis for a modified fatigue life prediction, the value is altered from 64.38 MPa for the whole series, to 63.83 MPa for small defects and to 49.29 MPa for large defects. The reason for the decrease in fatigue life, even for the small defects, is that the load bearing cross section is larger than the theoretical cross section, as seen in Table 9. The Defect-S-N curve is presented in Figure 44.
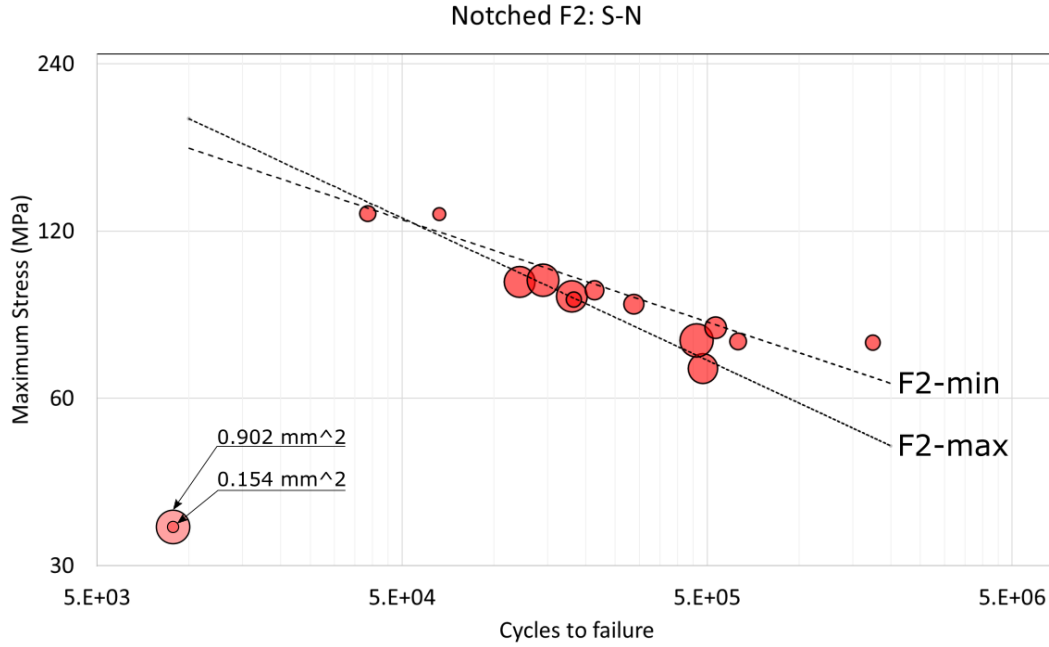
Figure 44: Bubble graph of the F2 S-N diagram.

A S-N curve were also created based on gas inclusion area, after the criterion presented in 3.1.3. This was done in the same fashion as in Table 11, where H denotes the gas inclusion defect, 1 represents Theoretical Area, 2 represents Real Area and 3 represents Load bearing Area. This yields the values presented in table 12. H3 is then chosen, based on the low scatter.

Table 12: Data from empirical analysis of S-N diagram based on gas inclusion area.

Graph	σ_{50} (Mpa)	T_σ	k	Defect range (mm^2)	Data points
$H1_{min}$	71.43	1.445	6.26	0.009 - 0.020	7
$H1_{max}$	54.70	1.621	3.86	0.020 - 0.031	6
$H2_{min}$	67.15	1.417	7.40	0.009 - 0.020	7
$H2_{max}$	48.78	1.673	3.70	0.020 - 0.031	6
$H3_{min}$	67.80	1.404	7.13	0.009 - 0.020	7
$H3_{max}$	49.96	1.655	3.76	0.009 - 0.031	6
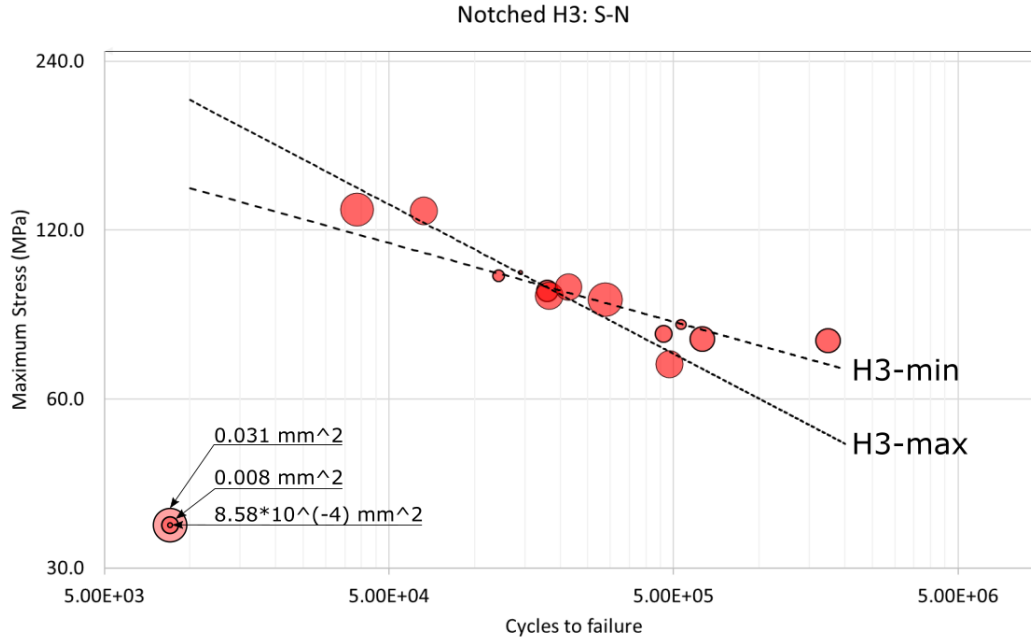
Figure 45: Bubble graph of the H3 S-N diagram.

Looking at the defects for the total series, the data presented in Table 13 are obtained. In the notched series, it is observed that the heat treated series had 9.13% higher area loss at geometry surface from gas inclusions, and 4.65% higher load bearing area loss from the (C-L)FC measurement, compared to the as-build series. When going from AB to HT in the smooth series, the defect increased by 96.15% with respect to gas inclusions and 99.45% with respect to (C-L)FC.

Table 13: Average defect size measured.

Series	Avg. gas inclusion area (μm^2)	Avg. (C-L)FC (μm^2)
Smooth, HT	16967	108272
Smooth, AB	8650	54286
Notched, HT	15925	474337
Notched, AB	14593	453254

The defect dependent S-N curves were also created for the smooth series, but without the experimental approach to determine the most suitable measurement method. Instead, it was assumed that the same method chosen for notched defect measurement would yield the most accurate results for smooth specimens as well. The F2 and H3 measurements were therefore conducted on both smooth series, as well as the notched as-build series, giving the results displayed in Table 14.

44

Table 14: Summary of chosen defect dependent S-N curves. S = Smooth, N = Notched, HT = Heat Treated and AB = As-Build.

Graph	σ_{50} (MPa)	T_σ	k	Defect range (mm^2)	Data pts.
$N, HT, F2_{min}$	63.83	1.557	5.43	0.15 - 0.40	8
$N, HT, F2_{max}$	49.29	1.512	3.91	0.73 - 0.90	5
$N, HT, H3_{min}$	67.80	1.404	7.13	0.01 - 0.02	7
$N, HT, H3_{max}$	49.96	1.655	3.76	0.01 - 0.03	6
$N, AB, F2_{min}$	39.90	1.370	4.12	0.08 - 0.21	6
$N, AB, F2_{max}$	36.67	2.569	3.75	0.50 - 1.09	5
$N, AB, H3_{min}$	40.42	1.728	4.52	0.00 - 0.01	5
$N, AB, H3_{max}$	40.12	1.472	3.97	0.01 - 0.04	6
$S, AB, F2_{min}$	67.66	2.341	4.52	0.03 - 0.05	4
$S, AB, F2_{max}$	67.79	1.330	4.12	0.06 - 0.10	4
$S, AB, H3_{min}$	61.80	3.410	3.87	0.00 - 0.00	4
$S, AB, H3_{max}$	65.01	1.482	3.95	0.01 - 0.02	4
$S, HT, F2_{min}$	76.15	6.835	3.43	0.06 - 0.08	4
$S, HT, F2_{max}$	110.73	1.856	4.95	0.08 - 0.24	4
$S, HT, H3_{min}$	113.93	1.899	5.62	0.00 - 0.01	4
$S, HT, H3_{max}$	68.81	4.728	2.99	0.02 - 0.04	4

3.4   Discussion

3.4.1   Failure mechanisms

As mentioned in Section 3.3.2, all fatigue cracks started from the surface. In the notched case, this was highly expected, since the stress concentration is vastly larger at the surface than anywhere else, as shown in Figure 28. Any small defect on the surface would amplify this even further. For example, if a local defect acts as a micro notch with a stress intensity factor of $K_t = 2.0$, it would double the stress in the region, which is already affected by the intended U-notch stress amplification (3.2.1). The combined stress intensity factor would therefore be $K_t = 2.0 \times 2.549 = 5.098$. Keeping this in mind, it is not surprising that the vast majority of the notched samples had multiple crack initiation sites, since the surface roughness of AM produced parts are known to yield high surface roughness, which in turn introduces a micro notch effect in several locations (2.2).

In the smooth samples, the stress distribution is more uniform over the cross section. While this removes some of the importance of surface as a crack initiation site, it is still known from theory that surface finish is the most critical parameter in fatigue life, even without a notch (2.3). Here, the crack initiation sites were few, often just one. It was observed that the critical defect were fairly large, while the overall surface roughness was substantially lower than that of the notched samples, as shown in Table 13. This difference in defect characteristics might influence the comparability of the sample series. While the area loss method used in this work might be suitable for the notched samples, the more purely defect driven $\sqrt{area}$-method is arguably better for the finer surface finish and more prominent defects observed in the smooth samples (2.2.6).

The reason for the difference in surface finish at the fracture plane, measured as area loss, can possibly be credited to the challenging production of the small features in the notched sample series (Figure 25). The deviation from design displayed in Figure 33 can be considered an argument in favor of this hypothesis.

3.4.2 Notch sensitivity

Since the fatigue results presented in Section 3.3.3 have an acceptable amount of data points, as well as low scatter indexes, it is reasonable to use this data for calculating notch sensitivity. First, K_f is calculated for both the as-build and heat treated series. See section 2.4.

$$K_{f,ab} = \frac{70.32}{42.29} = 1.663, \quad K_{f,ht} = \frac{110.41}{64.38} = 1.715$$

This allows for the calculation of the corresponding notch sensitivity (eq. 4):

$$q_{ht} = \frac{K_{f,ht} - 1}{K_t - 1} = \frac{1.715 - 1}{2.549 - 1} = 0.462$$

$$q_{ab} = \frac{K_{f,ab} - 1}{K_t - 1} = \frac{1.663 - 1}{2.549 - 1} = 0.428$$

The slightly higher notch sensitivity for the heat treated series could be a result of the increase in porosity, thus also an increase in gas inclusions close to the surface, as shown in Table 13. The slight increase in surface area loss displayed in the same table could also be a contributing factor to this. However, the increase in gas pores is considered a more reliable explanation, since the difference is higher, and also because it fits better with literature. It is reported that heat treatment tends to increase porosity and void size [6]. This can be explained by the expansion of the trapped gas in the part while the metal is softer than usual during the heating. On the other hand, if some of the gas inclusions is of irregular shapes, this heating might expand the void into a more spherical shape, thus reducing the notch effect.

The difference in stress levels at the surface, already discussed in Section 3.4.1, combined with the higher roughness of the notched samples, is assumed to affect the notch sensitivity. If the production of the smooth and notched samples produced the same surface finish at surface subjected to the maximum stress levels, it would arguably result in a lower notch sensitivity.

3.4.3 Defect dependent fatigue analysis

Since the defect measurements explained in Section 3.1.3 were done by hand, they introduce some degree of uncertainty. It is not believed that the values obtained are accurate enough for conclusive characterization of the various defect types, but the analysis preformed is intended to serve as an indicator of trends with various defects.

The defect dependent fatigue life predictions presented in Table 14 can be used to estimate some specific notch sensitivities. Using the scatter index as a quality measurement, it is obvious that some of the graphs could not be used for predictions. A limit of $T_\sigma < 2$ was chosen, excluding any graphs with a scatter index higher than this. For the defect dependent notch sensitivity to be considered, both the smooth and notched case had to satisfy this condition. This leaves the measurements $HT, F2_{max}$, $HT, H3_{min}$ and $AB, H3_{max}$. Determining the experimental value K_f:

$$K_{f,ht,f2,max} = \frac{110.73}{49.29} = 2.247, \quad K_{f,ht,h3,min} = \frac{113.93}{49.96} = 2.280$$

$$K_{f,ab,h3,max} = \frac{65.01}{40.12} = 1.620$$

Calculating the notch sensitivities, using Equation 4.

$$q_{ht,f2,max} = \frac{K_{f,ht,f2,max} - 1}{K_t - 1} = \frac{2.247 - 1}{2.549 - 1} = 0.805$$

$$q_{ht,h3,min} = \frac{K_{f,ht,h3,min} - 1}{K_t - 1} = \frac{2.280 - 1}{2.549 - 1} = 0.826$$

$$q_{ab,h3,max} = \frac{K_{f,ab,h3,max} - 1}{K_t - 1} = \frac{1.620 - 1}{2.549 - 1} = 0.400$$

Looking at the notch sensitivities obtained, it appears that the $HT, F2_{max}$ and $HT, H3_{min}$ measurements share large portions of their data points, since the values are so similar. However, examining the raw data, it is revealed that this is not the case.

The increase in notch sensitivity for large surface defects in heat treated samples are as expected, as it is known that the notched case experience much higher stress at the surface compared to smooth samples, thus amplifying the importance of surface roughness. While the $q_{ht,f2,max}$ value is quite reasonable, there are still some uncertainties to consider. The min and max separation were done relative to the series being examined, and not coordinated with the corresponding series used for notch sensitivity calculation. Therefore, it is a noticeable discrepancy between the the defect range of, for example, $N, HT, F2_{max}$ and $S, HT, F2_{max}$.

To further examine the trends of the notch sensitivity, some additional calculations were done. These were chosen from S-N curves with higher scatter index, but not higher than 2.60.

$$K_{f,ab,f2,max} = \frac{67.79}{36.67} = 1.849, \quad K_{f,ab,f2,min} = \frac{67.66}{39.90} = 1.696$$

$$q_{ab,f2,max} = \frac{K_{f,ab,f2,max} - 1}{K_t - 1} = \frac{1.849 - 1}{2.549 - 1} = 0.548$$

$$q_{ab,f2,min} = \frac{K_{f,ab,f2,min} - 1}{K_t - 1} = \frac{1.696 - 1}{2.549 - 1} = 0.449$$

These calculations support the claim that notch sensitivity increases with increasing surface defects, measured after the F2 model (Table 7).

The values for notch sensitivities after the H3 model appears counter intuitive. Comparing them to the notch sensitivities of the whole series from Section 4, it appears that large gas inclusions would reduce notch sensitivity in the as-build case, while small gas inclusions would nearly double the notch sensitivity in the heat treated case. However, when considering the effect of gas inclusions with respect to the stress distribution over the cross section, as shown in Figure 28 and 32, it becomes more reasonable. The gas inclusions were evaluated based on Biswal et al [8], where the FEM analysis were preformed for uniform stress distribution, which resembles the smooth case, but not the notched. Looking at Figure 46 and comparing it to the stress distribution over the cross section, it is clear that the gas inclusions are influencing the local stress intensity to a lesser degree in the notched case. For example, if a gas inclusion is located so that the surface of the inclusion is $0.15mm$ from the geometry surface, the local intensity factor before considering the gas inclusion would be about 2.0. The surface defects, on the other hand, would experience local stress intensity equal to the calculated maximum, namely $K_t = 2.549$. This means that gas inclusions and surface defects does not compete on equal terms. The stress intensity caused by surface defects are thus increased compared to gas inclusions.

In the smooth samples, this is not the case. Here, the stress intensity is close to uniform along the cross section. Keeping this in mind, it is logical that the smooth samples are more

affected by gas inclusions than the notched samples. Since notch sensitivity is dependent upon the relationship between the two, these results are considered in accordance with theory (2.3).
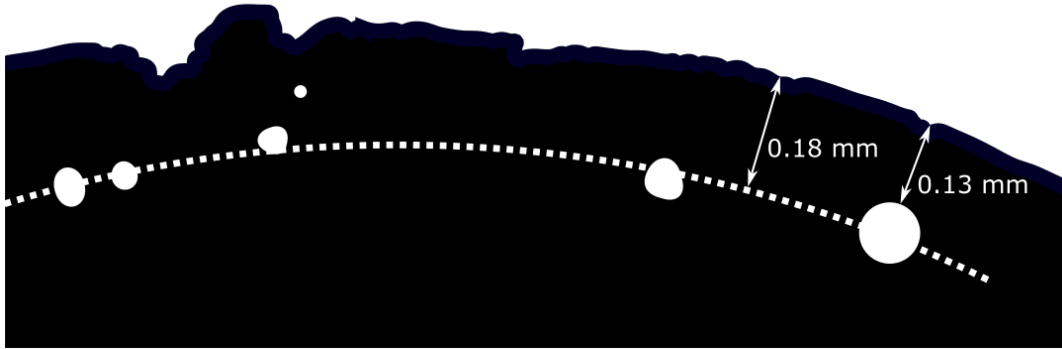
Figure 46: Measurement of typical distance between geometry surface and gas inclusions.

The reason for the consistent distance from surface to the gas inclusions, shown in Figure 46, is credited to the production method, and more specifically the interface between the shell layer and infill, as observed in multiple fracture surfaces, especially in Figure 34c. This is also illustrated in Figure 47. The *raster width* referred to in this figure is the with of the melting pool from the laser during production.
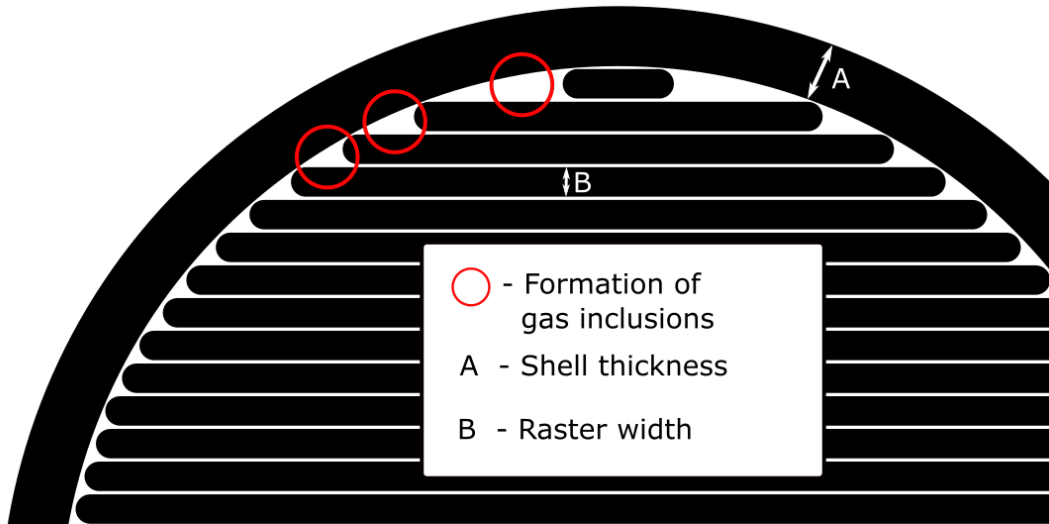
Figure 47: Simplified schematic of a SLM production layer.

3.4.4 Topology deviation

As highlighted in Section 3.3.1, the topology of the final samples deviated somewhat from the intended design. Evaluating this with the area deviation found during the fracture surface analysis, displayed in Table 9, it is assumed that the average topology were not as designed. Using the observed average area deviation, a real average radius (r_a) is calculated to be

$$A_a = 1.10A_t \rightarrow r_a = \sqrt{1.10r_t^2} = 2.622mm$$

where A_a is average area, A_t is theoretical area and the theoretical radius is $r_t = 2.5mm$. Evaluating the notched heat treated series, it was observed from raw data that there were two main divisions of area measurement, one averaging at 13.36% area deviation and the other at 8.08%. These area discrepancy divisions correlated perfectly with the F2 measurement. The corresponding radii are calculated to be

$$r_{min} = 2.599mm, \qquad r_{max} = 2.662mm$$

where r_{min} corresponds to the low area deviation group and r_{max} corresponds to the high area deviation group. Comparing the difference between these gives:

$$\Delta r = r_{max} - r_{min} = 0.063mm$$

One reason for this noticeable split in area, and subsequently average radius, could be that the crack initiated from an unintended notch, as illustrated in Figure 33. However, the observed distance from unintended notch to intended maximum stress intensity is measured to be $0.17mm$, which is substantially higher than Δr. Yet, during SEM imaging and fracture surface analysis, it was observed a correlation between high cross section area and apparent base initiated fracture (Figure 35). It could therefore be argued that the sample examined in OM (Figure 33) would have failed from the intended area, while other samples with a deeper, more prominent unintended notch failed from the base. This would bridge the gap between the observed trend in fracture surfaces and the calculated Δr.

The proposition that the samples with large defects in fact failed from a secondary notch, is somewhat supported by the defect dependent S-N curves, seen in Table 14 and Figure 44. Here it is observed that the log S - log N line is steeper for the large defects, recognized by low k value in the table, which is characteristic for sharper notches. The notion of an unintended notch as a secondary crack initiation point is therefore considered highly plausible.

3.5 Conclusion

The experiments performed provided values for notch sensitivity for both as-build and heat treated Al-Si-10Mg produced by SLM. These values were found to be

$$q_{ht} = 0.462, \quad q_{ab} = 0.428$$

for the two series. The defects were generally larger for heat treated samples, which might account for the slight difference in notch sensitivity. Through fractography analysis, it was fund that all cracks started from the surface. In the U-notched samples, the initiation were mainly from rough surface acting as micro notches. In the smooth samples, the dominant failure mechanism were lack of fusion. Further, a new approach to defect evaluation revealed some trends in the effect on fatigue life. Higher surface area loss were found to correlate with a reduction in fatigue strength, while the presence of gas inclusions were less consequential when considering notched geometry, compared to smooth geometry. Some defect dependent

notch sensitivities were calculated.

$$q_{ab, \ small \ defects} = 0.449, \quad q_{ab, \ large \ defects} = 0.548, \quad q_{ht, \ large \ defects} = 0.805$$

$$q_{ht, \ small \ gas \ inclusions} = 0.826, \quad q_{ht, \ large \ gas \ inclusions} = 0.400$$

Lastly, it was observed that the small dimensions of the notched geometry resulted in some reduction in dimensional accuracy from production, thus somewhat increasing the uncertainty of these results. This also introduced the possibility of a secondary, unintended, notch – which some of the samples might have failed from.

4 Developing a standard

To fully utilize the potential of AM, some improvement on production standards are needed. However, the amount of production parameters and the lack of understanding of these makes it hard to arrive at concrete specifications. Yet, some empiric data is available, both in literature and presented in this work, thus the author will suggest some parameters for the development of a standard in SLM production of Al-Si-10Mg.

4.1 Shell layer count

The shell layers are defined by the author as the number of geometry defining revolutions made before the infill process. The wall thickness is thus a multiplier of raster width, and can be described as

$$S = wn$$

where S is the shell thickness, w is the raster width and n is the shell layer count. See Figure 47. Note that it is assumed that the shell layer is a function of raster width.

As discussed in Section 3.4.3, the effect of gas inclusions is a function of gas inclusion size, distance from gas inclusion to geometry surface and the stress distribution over the cross section. While it is difficult to determine the exact distance from surface where the gas inclusions are of relevance compared to surface defects, it is known from literature that the limit for any gas inclusion to be affected by a surface effect is when $L < 4d$, where L is the distance from inclusion to the geometry surface and d is the gas inclusion diameter [8]. Using this as an upper limit, it is possible to determine a shell layer count so that the gas inclusions are never amplified by their proximity to the geometry surface. Substituting L with shell thickness S we get:

$$S < 4d \rightarrow wn < 4d \rightarrow n < \frac{4d}{w}$$

This represents the shell layer count which allows for the surface effect of the gas inclusions. To get the expression that excludes them, the equation has to be reversed. This gives

$$n > \frac{4d}{w}$$

where the shell layer count n is a natural number, d is the diameter of the gas inclusion evaluated and w is the raster width. Following this limit in production, it should be possible to minimize the effect of the largest gas inclusions.

5   Further work

By taking on a broader perspective and looking at the SLM production of aluminum alloys, the printing parameters should be studied further. Right now, it is very hard to predict the mechanical behaviour of a SLM produced aluminum alloy, or any alloy, solely based on input parameters in the production. Since the reported mechanical properties varies so much, SLM has after the authors best understanding a great potential with respect to tailoring materials for specific use [25].

5.1   Defect analysis

While the defect analysis conducted in this work did prove useful to reveal some trends, a more accurate and consequent approach is needed if the area loss method is to be relied upon for accurate predictions. To increase accuracy and reduce labor intensity, the author suggests the development of a computer vision based analysis. This way, a consistent maximum radius could be applied to the Caliper Surface Line and realistic Load Bearing Geometry (Figure 21), thus removing the uncertainty from the manual evaluation. It would also allow for evaluation of vastly bigger data sets, which in turn would allow for further developing the area loss defect evaluation. Further investigation into whether the area loss method is viable or not should be undertaken before such a big project is started.

References

[1] materials, properties and design. `https://www.princeton.edu/~maelabs/mae324/01/01_57.htm`. Accessed: 2018-12-11.

[2] petersons kt for circular specimen with u-notch. tension. `https://www.efatigue.com/castiron/stressconcentration/`. Accessed: 2018-12-07.

[3] researchgate. `https://www.researchgate.net/figure/The-Al-Si-phase-diagram-6_fig6_258390327`. Accessed: 2018-12-11.

[4] L. KATGERMAN TH. H. DE KEIJSER E. J. MITTEMEIJER N. M. VAN DER PERS A. BENDIJK, R. DELHEZ. Characterization of al-si-alloys rapidly quenched from the melt. *JOURNAL OF MATERIALS SCIENCE*, 15:2803–2810, 1980.

[5] H.V. Davies Atkinson. Fundamental aspects of hot isostatic pressing: An overview. *S. Metall and Mat Trans A*, 31A:2981–3000, 2000.

[6] Sara Bagherifard, Niccolò Beretta, Stefano Monti, Martina Riccio, Michele Bandini, and Mario Guagliano. On the fatigue strength enhancement of additive manufactured alsi10mg parts by mechanical and thermal post-processing. *Materials Design*, 145:28–41, 2018.

[7] Martin Baumers, Phill Dickens, Chris Tuck, and Richard Hague. The cost of additive manufacturing: machine productivity, economies of scale and technology-push. *Technological Forecasting and Social Change*, 102:193–201, 2016.

[8] Romali Biswal, Abdul Khadar Syed, and Xiang Zhang. Assessment of the effect of isolated porosity defects on the fatigue performance of additive manufactured titanium alloy. *Additive Manufacturing*, 23:433–442, 2018.

[9] F. C Campbell. *Metals Fabrication - Understanding the Basics*. ASM International, 2013.

[10] Kwai S. Chan, Marie Koike, Robert L. Mason, and Toru Okabe. Fatigue life of titanium alloys fabricated by additive layer manufacturing techniques for dental implants. *Metallurgical and Materials Transactions A*, 44(2):1010–1022, 2012.

[11] Eric Charkaluk and Victor Chastand. Fatigue of additive manufacturing specimens: A comparison with casting processes. *Proceedings*, 2(8), 2018.

[12] Mile B. Djurdjević, Srećko Manasijević, Zoran Odanović, and Natalija Dolić. Calculation of liquidus temperature for aluminum and magnesium alloys applying method of equivalency. *Advances in Materials Science and Engineering*, 2013:1–8, 2013.

[13] Christer W. Elverum and Torgeir Welo. On the use of directional and incremental prototyping in the development of high novelty products: Two case studies in the automotive industry. *Journal of Engineering and Technology Management*, 38:71–88, 2015.

[14] Vitus Holzinger Damien Buchbinder Erhard Brandl, Ulrike Heckenberger. Additive manufactured alsi10mg samples using selective laser melting (slm): Microstructure, high cycle fatigue, and fracture behavior. *Materials and Design*, 34:159–169, 2012.

[15] Luca Facchini, Emanuele Magalini, Pierfrancesco Robotti, and Alberto Molinari. Microstructure and mechanical properties of ti-6al-4v produced by electron beam melting of pre-alloyed powders. *Rapid Prototyping Journal*, 15(3):171–178, 2009.

[16] William E. Frazier. Metal additive manufacturing: A review. *Journal of Materials Engineering and Performance*, 23(6):1917–1928, 2014.

[17] Nan Kang, Pierre Coddet, Lucas Dembinski, Hanlin Liao, and Christian Coddet. Microstructure and strength analysis of eutectic al-si alloy in-situ manufactured using selective laser melting from elemental powder mixture. *Journal of Alloys and Compounds*, 691:316–322, 2017.

[18] K. Kempen, L. Thijs, J. Van Humbeeck, and J. P. Kruth. Mechanical properties of alsi10mg produced by selective laser melting. *Physics Procedia*, 39:439–446, 2012.

[19] Wei Li, Shuai Li, Jie Liu, Ang Zhang, Yan Zhou, Qingsong Wei, Chunze Yan, and Yusheng Shi. Effect of heat treatment on alsi10mg alloy fabricated by selective laser melting: Microstructure evolution, mechanical properties and fracture mechanism. *Materials Science and Engineering: A*, 663:116–125, 2016.

[20] Yukitaka Murakami. *Metal Fatigue: Effects of Small Defects and Nonmetallic Inclusions*. ELSEVIER SCIENCE, 2002.

[21] Jonathan Pegues, Michael Roach, R. Scott Williamson, and Nima Shamsaei. Surface roughness effects on the fatigue strength of additively manufactured ti-6al-4v. *International Journal of Fatigue*, 116:543–552, 2018.

[22] H. K. Rafi, N. V. Karthik, Haijun Gong, Thomas L. Starr, and Brent E. Stucker. Microstructures and mechanical properties of ti6al4v parts fabricated by selective laser melting and electron beam melting. *Journal of Materials Engineering and Performance*, 22(12):3872–3883, 2013.

[23] Robert R. Stephens Henry O. Fuchs Ralph I Stephens, Ali Fatemi. *Metal Fatigue in Engineering*. Wiley-interscience, 2 edition, 2000.

[24] S. M. J. Razavi, P. Ferro, F. Berto, and J. Torgersen. Fatigue strength of blunt v-notched specimens produced by selective laser melting of ti-6al-4v. *Theoretical and Applied Fracture Mechanics*, 97:376–384, 2018.

[25] S. Romano S. Beretta. A comparison of fatigue strength sensitivity to defects for materials manufactured by am or traditional processes. *International Journal of Fatigue*, 94:178–191, 2016.

[26] Klaus Schwab. *The Fourth Industrial Revolution*. Crown Publishing, 2017.

[27] S. L. Sing, J. An, W. Y. Yeong, and F. E. Wiria. Laser and electron-beam powder-bed additive manufacturing of metallic implants: A review on processes, materials and designs. *J Orthop Res*, 34(3):369–85, 2016.

[28] F. Berto S.M.J. Razavi, P. Ferro. Fatigue assessment of ti-6al-4v circular notched specimens produced by selective laser melting. *Metals*, 7:291, 2017.

[29] P. Ferro J. Torgersen F. Berto S.M.J. Razavi, G. Bordonaro. Porosity effect on tensile behavior of additively manufactured ti-6al-4v samples. *Proceedings of the Institution of Mechanical Engineers, Part C: Journal of Mechanical Engineering Science*.

[30] Jyoti Suryawanshi, K. G. Prashanth, S. Scudino, J. Eckert, Om Prakash, and U. Ramamurty. Simultaneous enhancements of strength and toughness in an al-12si alloy synthesized using selective laser melting. *Acta Materialia*, 115:285–294, 2016.

[31] Mary Kathryn Thompson, Giovanni Moroni, Tom Vaneker, Georges Fadel, R. Ian Campbell, Ian Gibson, Alain Bernard, Joachim Schulz, Patricia Graf, Bhrigu Ahuja, and Filomeno Martina. Design for additive manufacturing: Trends, opportunities, considerations, and constraints. *CIRP Annals*, 65(2):737–760, 2016.

[32] Sigmund A. Tronvoll, Christer W. Elverum, and Torgeir Welo. Dimensional accuracy of threads manufactured by fused deposition modeling. *Procedia Manufacturing*, 26:763–773, 2018.

[33] Ben Vandenbroucke and Jean-Pierre Kruth. Selective laser melting of biocompatible metals for rapid manufacturing of medical parts. *Rapid Prototyping Journal*, 13(4):196–203, 2007.

[34] T. Vilaro, C. Colin, and J. D. Bartout. As-fabricated and heat-treated microstructures of the ti-6al-4v alloy processed by selective laser melting. *Metallurgical and Materials Transactions A*, 42(10):3190–3199, 2011.

[35] F. Pyczak P. Staron S. Schumann N. Huber X. Larráyoz Izcara, A. Guirao Blank. Characterization and modeling of the influence of artificial aging on the microstructural evolution of age-hardenable alsi10mg(cu) aluminum alloys. *Materials Science and Engineering: A*, 610:46–53, 2014.

[36] Rei Mihara Masami Okada Yukitaka Murakami Yoichi Yamashita, Takao Murakami. Defect analysis and fatigue design basis for ni-based superalloy 718 manufactured by additive manufacturing. *Procedia Structural Integrity*, 7:11–18, 2017.

Sikkerhets- og kvalitetsgjennomgang av laboratorietester og verkstedsarbeid

Safety and Quality Evaluation of Activities in the Laboratory and Workshop

O NTNU

**Perleporten
Rev 10, 2018-Aug**

1 Identifikasjon - *Identification*	Dokumentnr. – *Document no.*:	
Kundenavn – *Customer name* Sondre Hafnor	Prosjektnavn – *Project name* Sayed Mohammed Javad Rezavi	Projektnr. – *Project no.* 81771033
Beskrivelse av arbeid – *Description of job* Preparing and imaging of fracture surfaces from fatigue testing		Dato – *Date* 05.02.2019

2 Projekt - *Team*

Prosjektleder og organisasjon – *Project manager and organisation*		Ansvarlig for instrumentering – *Responsible for instrumentation.*	
Leiestedsansvarlig – *Laboratory responsible*		Operatør – *Operator*	
Auditør for sikkerhets og kvalitetsgjennomgang – *Auditer for safety check*		Ansvarlig for styring av forsøk – *Responsible for running the experiment.*	
Ansvarlig for eksperimentelt faglig innhold – *Responsible for experimental and scientific content*		Ansvarlig for logging av forsøksdata – *Responsible for logging and storing experimental data*	
Ansvarlig for dimensjonering av last og trykkpåkjente komponenter – *Reponsible for dimensioning load bearing and pressurized components*		Ansvarlig for montering av testrigg – *Responsible for building the rig*	

3 Viktig!! – *Important!!*

J: Ja – *Yes* / N: Nei - *No*

Er arbeidsordren signert? – *Is the work order signed?*	No
Har operatøren nødvendig kurs/trening i bruk av utstyret? - *Has the operator the required courses/training on the equipment?*	Yes
Har operatøren sikkerhetskurs? (påbudt) – *Has the operator followed the safety courses? (mandatory)*	Yes
Kan jobben gjøres alene? - *Can the work be done alone?*	Yes
- Dersom ja, er det med visse forbehold (for eksempel, må bruke alarm, ha avtale med noen som kommer innom med jevne mellomrom eller lignende). Dette må vurderes i Seksjon 5.*If yes, the work may have to be done under special conditions (e.g. must use the alarm, have agreement with somebody coming back periodically or similar). This shall be evaluated in Section 5.*	No
Må en ekspert se på oppstart av eksperimentet? Does an expert have to check the start of the experiment?	No
- Dersom ja, hvem? *If yes, who?*	

4.1 Sikkerhet – *Safety* (Testen medfører – *The test contains*)

J: Ja – *Yes* / N: Nei - *No*

Stor last – *Big loads*	No	Brannfare – *Danger of fire*	No
Tunge løft – *Heavy lifting*	No	Arbeid i høyden – *Working at heights*	No
Hengende last – *Hanging load*	No	Hydraulisk trykk – *Hydraulic pressure*	No
Gasstrykk – *Gas pressure*	No	Vanntrykk – *Water pressure*	No
Høy temperatur – *High temperature*	No	Lav temperatur – *Low temperature*	No
Deler i høy hastighet – *Parts at high velocity*	No	Farlige kjemikalier – *Dangerous chemicals*	Yes
Sprutakselerasjon ved brudd – *Sudden acceleration at fracture/failure*	No	Forspente komponenter – *Pre-tensioned components*	No
Farlig støv – *Dangerous dust*	No	Kraftig støy – *Severe noise*	No
Klemfare – *Danger of pinching*	No	Roterende deler – *Rotating parts*	No

4.2 Påkrevet verneustyr – *Required safety equipment*

J: Ja – *Yes* / N: Nei - *No*

Briller (påbudt) – *Glasses (mandatory)*	No	Vernesko – *Safety shoes*	No
Hjelm – *Helmet*	No	Hansker – *Gloves*	Yes
Skjerm – *Screen*	No	Visir – *Visir*	No
Hørselsvern – *Ear protection*	No	Løfteredskap – *Lifting equipment*	No
Yrkessele, fallsele, etc. – *Harness ropes, other measures to prevent falling down.*	No		

<table>
<tr><td colspan="2" align="center">Sikkerhets- og kvalitetsgjennomgang av laboratorietester og verkstedsarbeid</td><td>NTNU
Perleporten</td></tr>
</table>

5.1 Beskrivelse av aktivitet – *Description of the activity (see Appendix)*

Vurdering skal være basert på en skriftlig prosedyre for bruk av maskinen. I enkelte tilfeller kan prosedyre bli beskrevet direkte i tabellen nedenfor.	*The evaluation shall be based on a written operating procedure for the machine. For simple cases the procedure can be directly described in the tables below.*

Nr.	Beskrivelse av aktivitet – *Description of activity*	Fare - *Danger*	Lov, forskrift o.l. – *Legal requirements*	Prosedyre nr. – *Procedure no.*	Sannsynlighet – *Probability*	Konsekvens –*Consequence*	Risiko – *Risk*
1	Cutting the samples	Cutting myself	NTNU – HMS		2	A	A2
2	Imageing with SEM	Damage to equipment	NTNU – HMS		3	C	C3

5.2 Korrigerende Tiltak – *Corrective Actions*

Nr.	Korrigerende tiltak – Corrective action	Sannsynlighet – *Probability*	Konsekvens – *Consequence*	Risiko – *Risk*	Utført dato – *Date of action*
2	Taking great care to follow detailed procedure, even after several tests	1	B	B1	03.02.2019

Sikkerhets og kvalitetsgjennomgang av laboratorietester og verkstedsarbeid

NTNU
Perleporten

5.3 Feilkilder – *Reasons for mistakes/errors*
Sjekkliste: Er følgende feilkilder vurdert? – Check list: Is the following considered?   J: Ja – *Yes* / N: Nei - *No*

Tap av strøm – *Loss of electricity*		Overspenning – *Voltage surge*	
Elektromagnetisk støy – *Electromagnetic noise*		Manglende aggregatkapasitet av hydraulikk – *Insufficient power of the machine*	
Jordfeil – *Electrical earth failure*		Vannsprut – *Water jet*	
Ustabilt trykk av hydraulikk/kraft – *Unstable pressure or hydraulic force*		Tilfeldig avbrudd av hydraulikk/kraft – *Unintended interruption of power supply*	
Last-/ forskyvnings grenser etablert ? – *Are load and displacement limits established?*		Lekkasjer (slanger/koblinger, etc.) – *Leakage of pipes, hoses, joints, etc.*	
Mulige påvirkninger fra andre aktiviteter – *Possible interference from other activities*		Mulige påvirkninger på andre aktiviteter – *Possible interference towards other activities*	
Problemer med datalogging og lagring – *Troubles in loading and storage*		Brann i laboratoriet – *Fire in the laboratory*	

6 Kalibreringsstatus for utstyr – *Calibration of equipment*
(ex: load cell, extensometer, pressure transducer, etc)

I.D.	Utstyr - *Equipment*	Gyldig til (dato) – *Valid until (date)*

7 Sporbarhet – *Tracebility*

Eksisterer – Is there	J: Ja – *Yes* / N: Nei - *No*
Er alle prøvematerialene kjente og identifiserbare? – *Are all experimental materials known and traceable?*	
Eksisterer det en plan for markering av alle prøvene? – *Is there a plan for marking all specimens?*	
Er dataloggingsutstyret identifisert? – *Is the data aquisition equipment identified?*	
Er originaldata lagret uten modifikasjon? – *Are the original data stored safely without modification?*	
Eksisterer det en backup-prosedyre? – *Is there a back-up procedure for the data (hard disk crash)?*	
Eksisterer det en plan for lagring av prøvestykker etter testing? – *Is there a plan for storing samples after testing?*	
Eksisterer en plan for avhending av gamle prøvestykker? – *Is there a plan for disposing of old samples?*	

8 Kommentarer – *Comments*

9 Signaturer – *Signatures*
Godkjent (dato/sign) – Approved (date/signature)

Prosjektleder – P*roject leader*	Verifikatør – *Verifier*	Godkjent – *Approved by*

Sannsynlighet vurderes etter følgende kriterier:
Probability shall be evaluated using the following criteria:

Svært liten Very unlikely 1	Liten Unlikely 2	Middels Probable 3	Stor Very Probable 4	Svært stor Nearly certain 5
1 gang/50 år eller sjeldnere – *Once per 50 years or less*	1 gang/10 år eller sjeldnere – *Once per 10 years or less*	1 gang/år eller sjeldnere – *Once a year or less*	1 gang/måned eller sjeldnere – *Once a month or less*	Skjer ukentlig – *Once a week*

Konsekvens vurderes etter følgende kriterier:
Consequence shall be evaluated using the following criteria:

Gradering – *Grading*	Menneske – *Human*	Ytre miljø, Vann, jord og luft – *Environment*	Øk/materiell – *Financial/Material*	Omdømme – *Reputation*
E **Svært Alvorlig** – ***Very critical***	Død – Death	Svært langvarig og ikke reversibel skade – *Very prolonged, non-reversible damage*	Drifts- eller aktivitetsstans >1 år. – *Shutdown of work >1 year.*	Troverdighet og respekt betydelig og varig svekket – *Trustworthiness and respect are severely reduced for a long time.*
D **Alvorlig** – ***Critical***	Alvorlig personskade. Mulig uførhet. – *May produce fatality/ies*	Langvarig skade. Lang restitusjonstid – *Prolonged damage. Long recovery time.*	Driftsstans > ½ år Aktivitetsstans i opp til 1 år – *Shutdown of work 0,5-1 year.*	Troverdighet og respekt betydelig svekket – *Trustworthiness and respect are severely reduced.*
C **Moderat** – ***Dangerous***	Alvorlig personskade. – *Permanent injury, may produce serious health damage/sickness*	Mindre skade og lang restitusjonstid – *Minor damage. Long recovery time*	Drifts- eller aktivitetsstans < 1 mnd – *Shutdown of work < 1 month.*	Troverdighet og respekt svekket – *Troverdighet og respekt svekket.*
B **Liten** – ***Relatively safe***	Skade som krever medisinsk behandling – *Injury that requires medical treatment*	Mindre skade og kort restitusjonstid – *Minor damage. Short recovery time*	Drifts- eller aktivitetsstans < 1uke – *Shutdown of work < 1 week.*	Negativ påvirkning på troverdighet og respekt – *Negative influence on trustworthiness and respect.*
A **Siker** - **Safe**	Injury that requires first aid	Insignificant damage. Short recovery time	Shutdown of work < 1day	

Risikoverdi = **Sannsynlighet X Konsekvenser**
Beregn risikoverdi for menneske. IPM vurderer selv om de i tillegg beregner risikoverdi for ytre miljø, økonomie/ material og omdømme. I så fall beregnes disse hver for seg.

Risk = **Probability X Consequence**
Calculate risk level for humans. IPM shall evaluate itself if it shall calculate in addition risk for the environment, economic/material and reputation. If so, the risks shall be calculated separately.

Risikomatrisen

Risk Matrix

I risikomatrisen er ulike grader av risiko merket med rød, gul eller grønn:

Rød: Uakseptabel risiko. Tiltak skal gjennomføres for å redusere riskoen.

Gul: Vurderingsområde. Tiltak skal vurderes.

Grønn: Akseptabel risiko. Tiltak kan vurderes ut fra andre hensyn.

Når risikoverdien havner på rødt felt, skal altså enheten gjennomføre tiltak for å redusere risikoen. Etter at tiltak er iverksatt, skal dere foreta ny risikovurdering for å se om risikoen har sunket til akseptabelt nivå.

For å få oversikt over samlet risiko: Skriv risikoverdi og aktivitetens IDnr. i risikomatrise (docx) / risikomatrise (odt). Eksempel: Aktivitet med IDnr. 1 har fått risikoverdi 3D. I felt 3D i risikomatrisen skriver du IDnr. 1. Gjør likedan for alle aktiviteter som har fått en risikoverdi. En annen måte å skaffe oversikt på, er å fargelegge feltet med risikoverdien i skjemaet for risikovurdering. Dette tydeliggjør og gir samlet oversikt over riskoforholdene. Ledelse og brukere får slik et godt bilde av risikoforhold og hva som må prioriteres.

In the risk matrix different degrees of risk are marked with red, yellow or green;

Red: Unacceptable risk. Measures shall be taken to reduce the risk.

Yellow: Assessment Area . Measures to be considered.

Green: Acceptable risk. Measures can be evaluated based on other considerations.

When a risk value is red, the unit shall implement measures to reduce risk. After the action is taken, you will make a new risk assessment to see if the risk has decreased to acceptable levels.

To get an overview of the overall risk: Write the risk value and the task ID no . the risk matrix (docx) / risk matrix (odt) . Example : Activity with ID no . 1 has been risk value 3D. In the field of 3D risk matrix type ID no . 1 Do the same for all activities that have been a risk . Another way to get an overview is to color the field of risk value in the form of risk assessment . This clarifies and gives overview of the risk factors . Management and users get such a good picture of the risks and what needs to be prioritized.

KONSEKVENS	Svært alvorlig	E1	E2	E3	E4	E5
	Alvorlig	D1	D2	D3	D4	D5
	Moderat	C1	C2	C3	C4	C5
	Liten	B1	B2	B3	B4	B5
	Svært liten	A1	A2	A3	A4	A5
		Svært liten	Liten	Middels	Stor	Svært stor
		SANNSYNLIGHET				

Prinsipp over akseptkriterium. Forklaring av fargene som er brukt i risikomatrisen.

Farge		Beskrivelse
Rød		Uakseptabel risiko. Tiltak skal gjennomføres for å redusere risikoen.
Gul		Vurderingsområde. Tiltak skal vurderes.
Grønn		Akseptabel risiko. Tiltak kan vurderes ut fra andre hensyn.

_____

Til Kolonnen "Korrigerende Tiltak":

Tiltak kan påvirke både sannsynlighet og konsekvens. Prioriter tiltak som kan forhindre at hendelsen inntreffer, dvs sannsynlighetsreduserende tiltak foran skjerpende beredskap, dvs konsekvensreduserende tiltak.

For Column "Corrective Actions"
Corrections can influence both probability and consequence. Prioritize actions that can prevent an event from happening.

_____

Oppfølging:

Tiltak fra risikovurderingen skal følges opp gjennom en handlingsplan med ansvarlige personer og tidsfrister.

Follow Up
Actions from the risk evaluation shall be followed through by an action plan with responsible persons and time limits.

Etterarbeid #

- Gå gjennom aktiviteten/prosessen på nytt.
- Foreta eventuell ny befaring av aktiviteten/prosessen for enten a) å få bekreftet at risikoverdiene er akseptable eller b) for å justere risikoverdiene.
- Gå gjennom, vurder og prioriter tiltak for å forebygge uønskede hendelser. Først skal dere prioritere tiltak som reduserer sannsynlighet for risiko. Dernest skal dere ta for dere tiltak som reduserer risiko for konsekvenser.
- Tiltakene skal føres inn i handlingsplanen. Skriv fristen for å gjennomføre tiltaket (dato, ikke tidsrom) og navn på den / de som har ansvar for tiltakene.
- Foreta helhetsvurdering for å avgjøre om det nå er akseptabel risiko.
- Ferdig risikovurdering danner grunnlag for å utarbeide lokale retningslinjer og HMS-dokumenter, opplæring og valg av sikkerhetsutstyr.
- Ferdig risikovurdering og eventuelle nye retningslinjer gjøres kjent/tilgjengelig for alle involverte.
- Sett eventuelt opp kostnadsoverslag over planlagte tiltak.